A FINITE-ELEMENT APPROACH TO THE ANALYSIS OF TANGENTIALLY POLARIZED PIEZOELECTRIC-CERAMIC FREE-FLOODED CYLINDER TRANSDUCERS

Max R. Knittel, et al

Naval Undersea Center
San Diego, California

July 1974

NAVAL UNDERSEA CENTER, SAN DIEGO, CA. 92132

AN ACTIVITY OF THE NAVAL MATERIAL COMMAND

ROBERT H. GAUTIER, CAPT, USN
Commander

Wm. B. McLEAN, Ph.D.
Technical Director

ADMINISTRATIVE STATEMENT

The work in this report, performed from July through November 1973, was sponsored by the Naval Ship Systems Command, PMS 302-42, under Sub-Project SF 11-121-703, Task 14070.

ACKNOWLEDGEMENTS

The authors wish to express their appreciation to J. T. Hunt of Hydrospace-Challenger, Inc. and M. Carlson of NUC, Code 601, for their technical assistance.

UNCLASSIFIED

SECURITY CLASSIFICATION OF THIS PAGE (When Data Entered)

REPORT DOCUMENTATION PAGE		READ INSTRUCTIONS BEFORE COMPLETING FORM
1 REPORT NUMBER NUC TP 412	2 GOVT ACCESSION NO	3 RECIPIENT'S CATALOG NUMBER AD-783031
4 TITLE (and Subtitle) A FINITE-ELEMENT APPROACH TO THE ANALYSIS OF TANGENTIALLY POLARIZED PIEZOELECTRIC-CERAMIC, FREE-FLOODED CYLINDER TRANSDUCERS		5 TYPE OF REPORT & PERIOD COVERED Research report July - November 1973 6 PERFORMING ORG. REPORT NUMBER
7 AUTHOR(s) Max R. Knittel and Don Barach		8 CONTRACT OR GRANT NUMBER(s)
9 PERFORMING ORGANIZATION NAME AND ADDRESS Naval Undersea Center San Diego, Ca. 92132		10 PROGRAM ELEMENT PROJECT, TASK AREA & WORK UNIT NUMBERS Sub-Project SF 11-121-703, Task 14070
11 CONTROLLING OFFICE NAME AND ADDRESS Naval Ship Systems Command Washington, D. C. 20360		12 REPORT DATE July 1974 13 NUMBER OF PAGES 54
14 MONITORING AGENCY NAME & ADDRESS(if different from Controlling Office)		15 SECURITY CLASS (of this report) UNCLASSIFIED 15a DECLASSIFICATION DOWNGRADING SCHEDULE

16 DISTRIBUTION STATEMENT (of this Report)

Approved for public release; distribution unlimited.

17 DISTRIBUTION STATEMENT (of the abstract entered in Block 20, if different from Report)

18 SUPPLEMENTARY NOTES

19 KEY WORDS (Continue on reverse side if necessary and identify by block number)

transducers
free-flooded cylinder
finite-element method
acoustic radiation
piezoelectric ceramics

20 ABSTRACT (Continue on reverse side if necessary and identify by block number)

An approximation method is presented for solving the equations of motion that describe the vibration of a tangentially polarized piezoelectric-ceramic, staved, free-flooded cylinder transducer immersed in an infinite acoustic fluid medium. The mathematical model that is developed uses the finite-element method to calculate the vibrational characteristics of the elastic cylinder and the

DD FORM 1 JAN 73 1473 EDITION OF 1 NOV 65 IS OBSOLETE

UNCLASSIFIED

SECURITY CLASSIFICATION OF THIS PAGE (When Data Entered)

20. ABSTRACT (Cont.)

acoustic pressure field of that portion of the fluid which closely surrounds the cylinder out to a spherical surface. Analytical methods are used to obtain the boundary conditions for the spherical surface. This technique can be used to predict the transducer's complex electrical impedance, transmitting voltage response, and radiated power as functions of frequency. The vertical directivity pattern and displacement distribution on the cylinder can also be calculated for a given frequency. The inputs and outputs of the three computer programs that implement this mathematical modeling technique are discussed. Experimental validation of theoretical predictions are given for three example cylinders.

SUMMARY

PROBLEM

Develop a mathematical model that accurately describes the electrical and acoustical response of a tangentially polarized piezoelectric-ceramic, staved, free-flooded cylinder transducer. Implement this formulation in a package of computer programs that, from a set of user-specified dimensions and parameters, will automatically produce plots of the complex electrical impedance and transmitting voltage response as functions of frequency and, at any selected frequency, will calculate the vertical directivity pattern and cylinder displacement distribution. Compare the predicted response of a cylinder to that measured experimentally.

RESULTS

A finite-element approach was taken to the problem of solving the equations of motion for a tangentially polarized, piezoelectric-ceramic free-flooded cylinder immersed in an infinite acoustic fluid medium. The use of finite-element techniques makes it possible to predict the broadband response of the transducer. Three computer programs are used in the analysis: (1) a data generation program which produces the necessary finite-element input information; (2) an instruction program for the MARTSAM finite-element structural analysis and matrix system program; and (3) a program which solves the matrix equations that approximate the fluid-loaded cylinder's equations of motion for the electrical impedance, transmitting voltage response, and radiated power as functions of frequency. In addition, for a given frequency, the vertical directivity pattern and cylinder displacement distribution can be calculated. The ability of the mathematical model to accurately predict the in-air and in-water responses of free-flooded cylinders was shown by comparing the theoretical predictions to the experimentally measured responses of three cylinders.

CONTENTS

1 INTRODUCTION

The free-flooded cylinder transducer offers several distinct advantages over other types of underwater sonar projectors. Free-flooded cylinders have good power-to-weight ratios and bandwidths and are also, as their name implies, automatically pressure compensated for any change in operating depth. They are, therefore, nearly depth insensitive and have broad applications whenever a need arises for high-power sonar projectors with deep depth requirements or for sonar projectors with very broad bandwidths.

Acoustic propagation studies such as Project Artemis and LORAD have shown the advantages that deep acoustic installations offer over near-surface locations. Most types of transducers, such as the longitudinal vibrator, moving coil, or piezoelectric disk, require internal pressure compensation to keep the exterior ambient pressure from damaging the device or at least to prevent the response from greatly varying with changes in depth. This also provides a high degree of desired acoustic decoupling from the medium and transducer housing case at the back or inside of the radiating surface. Typical pressure compensation devices are pressure-release materials such as air or other gases, corprene, onionskin paper, Min-K and Sonite. Compliant tubes have also found great use as pressure-release devices, particularly in low-frequency bender-bar transducers. Most of these devices, however, lose their dynamic compliance under prolonged exposure to high pressure, are depth limited, or in the case of gas compensation, need complex external equipment.

As one solution to this problem, the free-flooded ring cylinder was developed. Initially, free-flooded cylinders were cast in one piece of piezoelectric ceramic and were radially polarized. These transducers used the K_{31} coupling of the electric and elastic fields. The use of vertically striped electrodes made it possible to polarize the solid cylinder in an approximate alternating tangential polarization; this allowed the use of the higher K_{33} coupling.

When lower frequency use was desired and the larger cylinders became difficult to fabricate in a single piece, a segmented or staved construction was designed (Ref. 1). This construction allowed the full use of the K_{33} coupling. Each stave was cast and electroded separately and then glued into a cylindrical configuration. A drawing of a typical tangentially polarized, free-flooded cylinder is shown in Fig. 1.

Free-flooded cylinders have been analyzed in the past with several different mathematical methods (Refs. 2-9). These techniques, however, often could not predict the broadband response of the cylinder because of inadequacies in the vibrational models of the structure. Finite-element techniques have been used to develop very accurate models for the cylinder that can predict the in-air response of the cylinder over a wide frequency band. These models have been experimentally validated through the use of holographic interferometry (Ref. 10). A finite-element model of a tangentially polarized-ceramic cylinder has been combined with an acoustic radiation program with good success (Ref. 11). In this analysis, finite-element techniques were used to calculate the normal velocities on the boundaries of the cylinder. Then the Helmholtz integral radiation program CHIEF (Ref. 12)

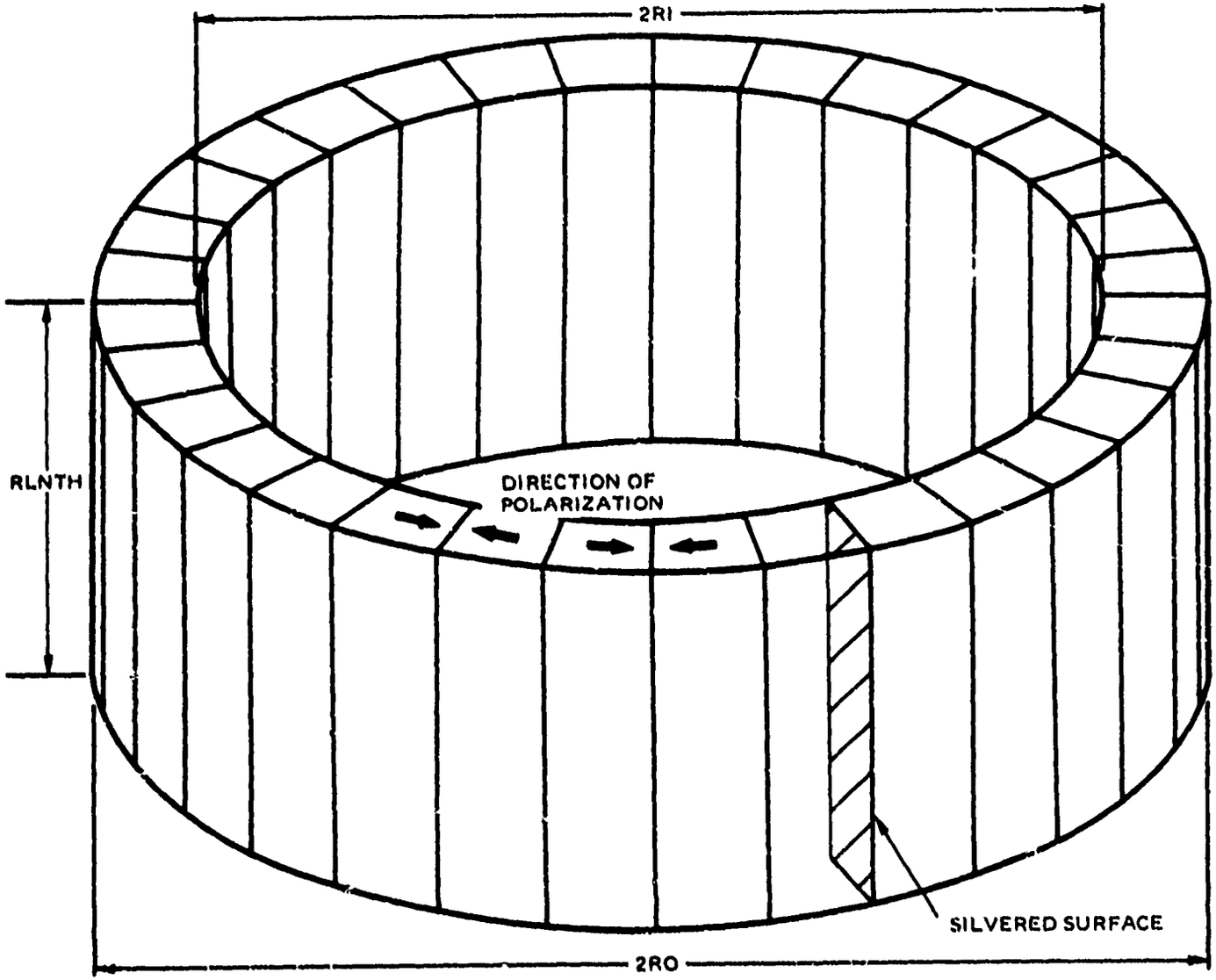

Figure 1. Tangentially polarized, piezoelectric-ceramic, free-flooded cylinder transducer.

was used to calculate the acoustic radiation impedance and the pressure at points in the near and far-fields at each driving frequency.

This last technique, although successful, is limited in its applications due to the necessity for numerically evaluating numerous and expensive integrals. The method that is developed in this report uses finite-element techniques as the mathematical approximation scheme for the elastic, piezoelectric-ceramic structure. Finite-element techniques are also used to mathematically model the acoustic fluid within a spherical surface which encloses the cylinder. Boundary conditions which are simple ratios of Hankel functions can now be applied to the spherical surface to give the mathematical appearance of a transducer immersed in an infinite acoustic fluid medium (free-field response). No numerical integrations are performed for the acoustic radiation part of the problem since the wave equation separates on a spherical surface when the pressures and normal velocities are expanded in spherical harmonic series.

Section 2 of this report presents the derivation of the matrix equations that represent the equations of motion of a free-flooded cylinder. Techniques for calculating both the cylinder's in-air and in-water responses are given.

Section 3 describes the computer programs that have been developed to implement the mathematical techniques described in Section 2. From a set of user-specified dimensions and parameters, three programs automatically generate the necessary finite-element idealizations for the cylinder and surrounding sphere of acoustic fluid, set up the required matrix equations, and then calculate the complex electrical impedance, transmitting voltage response and radiated power as functions of frequency. In addition, at any frequency, the vertical directivity pattern and the displacement distribution on the cylinder can be calculated.

Section 4 compares the theoretically calculated and experimentally measured responses of three free-flooded cylinder transducers. Comparisons are made between the in-air resonance and antiresonance frequencies, electrical capacitance, in-water electrical impedance, transmitting voltage response, and directivity patterns. Predictions are made for maximum source level and maximum radiated power at selected frequencies. The difficulties involved in predicting the response of a ceramic cylinder housed in a castor-oil-filled rubber and brass case by means of a mathematical model for only the bare ceramic cylinder are discussed.

2 FORMULATION

All of Euclidean 3-space is divided into two regions, R_1 and R_2 (Fig. 2). Region R_1 has a finite volume and contains all sources of sound; i.e., R_1 contains the free-flooded cylinder and a portion of the acoustic fluid. This region is bounded by the spherical surface S_1. Region R_2 is infinite in extent and is filled with a homogeneous acoustic fluid. The outward-drawn normal from a point ξ on surface S_1 is defined as n_ξ. The vector $\underline{d}(x,\xi)$ is the distance from a point ξ on S_1 to the field point x in region R_2. The point $\bar{x}$ is interior

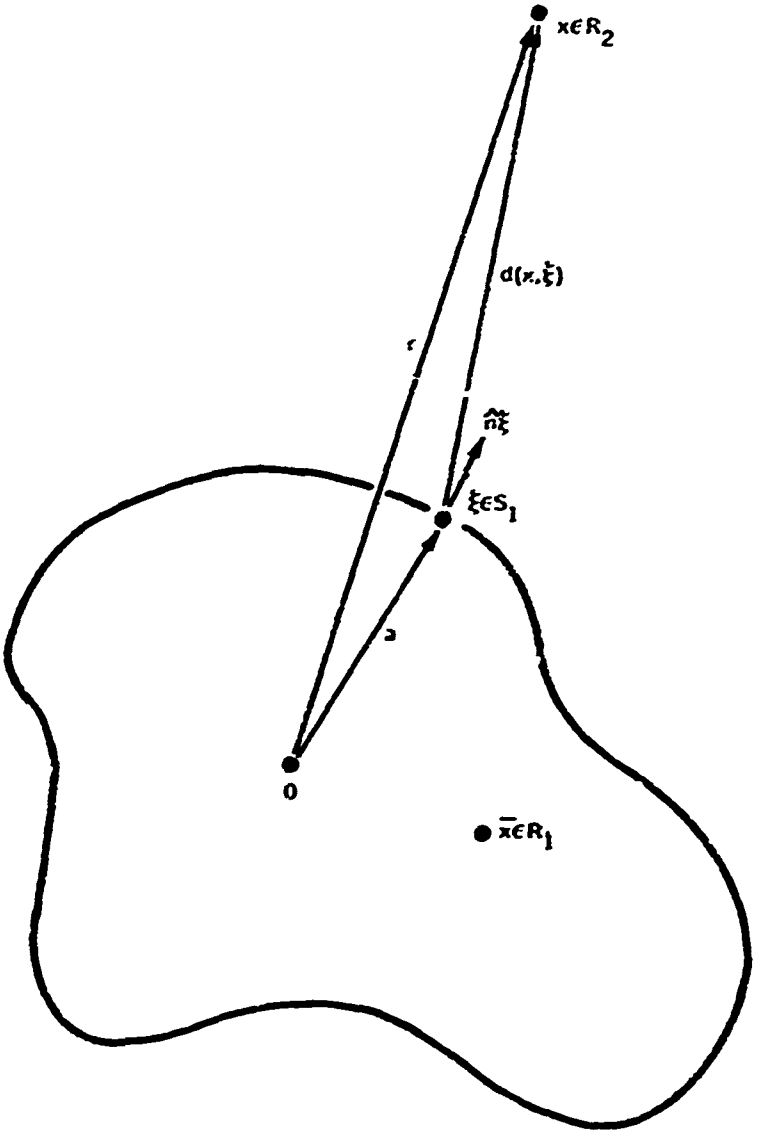

Figure 2. Euclidean 3-space divided into two regions, R_1 and R_2, by the closed surface S_1. x is a point in R_2, $\bar{x}$ a point in R_1, and ξ a point on S_1.

to S_1 in region R_1. Because the surface S_1 is spherical, simple analytical expressions can be found for the relationship between the surface pressures and normal velocities. This acoustic radiation impedance is the boundary condition that must be applied to the equations of region R_1 to yield the interaction of region R_1 with region R_2. Hence, the solution of the coupled structure-vibration/acoustic-radiation problem can be reduced to a system of boundary-value equations whose spatial domain is now a finite volume. A more detailed explanation of this formulation can be found in Ref. 13. An approximation method is now used to solve the equations of region R_1 subject to the analytical boundary conditions for surface S_1. This approximation scheme utilizes the finite-element method (Refs. 14-16).

In the finite-element formulation, the equations of motion for an elastic solid can be written in the matrix form

$$[M_S]\{\ddot{u}\} + [K_S]\{u\} = \{U\}\ , \tag{1}$$

where $[M_S]$ is the structural mass matrix, $[K_S]$ the structural stiffness matrix, $\{U\}$ the generalized nodal-point forces, and $\{u\}$ the nodal-point displacements. The derivative $\ddot{u}$ is defined as $\frac{\partial^2 u}{\partial t^2}$. The structural mass matrix is defined by

$$[M_S] \equiv \rho' \int_V [N']^T [N']\, dV\ , \tag{2}$$

where ρ' is the density of the piezoelectric ceramic and $[N']$ the structural-element interpolation function. The structural stiffness matrix is defined by

$$[K_S] \equiv \int_V [B']^T [D]\, [B']\, dV\ , \tag{3}$$

where $[B']$ is the matrix of derivatives of the structural-element interpolation function (the matrix that relates the strains to the nodal-point displacements), and $[D]$ denotes the elasticity matrix containing the appropriate material properties.

The generalized nodal-point forces can be written as the sum of two forces,

$$\{U\} = \{P\} + \{F_S\}\ . \tag{4}$$

where $\{P\}$ is a vector consisting of the nodal-point forces arising from the fluid pressure on the fluid–structure interfaces, and $\{F_S\}$ is a vector consisting of externally applied nodal-point forces (in this case, an electrical forcing function applied to the piezoelectric structure via a sinusoidally varying charge).

Similarly, the equations of motion which govern the behavior of the acoustic fluid in region R_1 are formulated in Refs. 17 and 18 as

$$[M_f]\{\ddot{p}\} + [K_f]\{p\} = \{C\}\ , \tag{5}$$

where $[M_f]$ is the fluid mass matrix, $[K_f]$ the fluid stiffness matrix, $\{C\}$ the generalized nodal-point forces, and $\{p\}$ the nodal-point pressures. Again, $\ddot{p}$ is defined as $\frac{\partial^2 p}{\partial t^2}$. The fluid mass matrix is defined by

$$[M_f] \equiv \frac{1}{c^2} \int_V [N]^T [N]\, dV\ , \tag{6}$$

where c is the speed of sound in the fluid and [N] the fluid-element interpolation function. The fluid stiffness matrix is defined by

$$[K_f] \equiv \int_V [B]^T [B] \, dV \ , \tag{7}$$

where [B] is the matrix of derivatives of the fluid-element interpolation function.

The generalized acoustic fluid nodal-point forces can also be written as the sum of two forces.

$$\{C\} = \{S\} + \{F_f\} \ , \tag{8}$$

where $\{S\}$ is a vector consisting of the nodal-point forces due to the acceleration of the boundaries of the elastic structure, and $\{F_f\}$ is a vector consisting of the nodal-point forces that arise from the interaction between the acoustic fluid in region R_1 and the acoustic fluid in the infinite exterior region R_2.

If the pressure interpolation function $N_i(x,y,z)$ for the acoustic fluid elements is defined as

$$p(x,y,z) = \sum_i N_i (x,y,z) \, p_i \ , \tag{9}$$

where p_i is the pressure at the i^{th} node and $p(x,y,z)$ is the pressure anywhere in the element, then Ref. 17 defines the fluid forces at node i as

$$(S)_i = \sum_{\text{elements}} \left[\int_S N_i \frac{\partial p}{\partial n} \, dS \right] \ , \tag{10}$$

where $\frac{\partial p}{\partial n}$ is the normal derivative of the pressure. Using the boundary condition

$$\frac{\partial p}{\partial n} = -\rho \dot{v}^n \ , \tag{11}$$

where v^n is the normal velocity of the fluid, Eq. (10) can be written as

$$(S)_i = -\rho \sum_{\text{elements}} \left[\int_S N_i \dot{v}^n \, dS \right] . \tag{12}$$

But $\hat{v}^n$ itself can be written in terms of the nodal-point accelerations as

$$\hat{v}^n = \sum_j N'_j \ddot{u}_j \quad , \tag{13}$$

where N'_j is the appropriate structural-element interpolation function for the normal displacement at the structure–fluid boundary, and $\ddot{u}_j$ is the acceleration of the j^{th} nodal point of the structure. Combining Eqs. (12) and (13), (S_i) now has the form

$$(S)_i = -\rho \sum_{\text{elements}} \sum_j \left[\int_S N_i N'_j \ddot{u}_j \, dS \right] \quad . \tag{14}$$

Similarly, the fluid-structure forcing function in Eq. (4) can be written as

$$(F)_i = \sum_{\text{elements}} \sum_j \left[\int_S N'_i N_j p_j \, dS \right] \quad . \tag{15}$$

The force terms $(S)_i$ and $(F)_i$ are the coupling between the acoustic fluid and the elastic structure. Comparing Eqs (14) and (15) reveals that by defining a coupling matrix $[T]$ such that

$$(T)_{i,j} = \sum_{\text{elements}} \left[\int_S N'_i N_j \, dS \right] \quad , \tag{16}$$

Eqs. (14) and (15) can be written in matrix form as

$$\{S\} = -\rho [T]^T \{\ddot{u}\} \quad , \tag{17}$$

and

$$\{P\} = [T] \{p\} \quad . \tag{18}$$

The combined structure-vibration/acoustic-radiation problem can now be written as two sets of coupled equations. The structure equations of motion appear as

$$[M_s] \{\ddot{u}\} + [K_s] \{u\} = [T] \{p\} + \{F_s\} \quad , \tag{19}$$

and the fluid equations appear in the form

$$[M_f] \{\ddot{p}\} + [K_f] \{p\} = -\rho [T]^T \{\ddot{u}\} + \{F_f\} \quad . \tag{20}$$

IN-AIR STRUCTURAL RESPONSE

The structure being considered here is composed of a material having not only elastic properties but piezoelectric properties as well. Reference 19 formulates the equations of

motion for a piezoelectric solid. The assembled set of structural equations can be written in the form

$$\begin{bmatrix} M_{uu} & 0 \\ 0 & 0 \end{bmatrix} \begin{Bmatrix} \ddot{u} \\ \ddot{\nu} \end{Bmatrix} + \begin{bmatrix} K_{uu} & K'_{u\nu} \\ K'_{\nu u} & K'_{\nu\nu} \end{bmatrix} \begin{Bmatrix} u \\ \nu \end{Bmatrix} = \begin{Bmatrix} 0 \\ Q \end{Bmatrix} , \tag{21}$$

where $\{\nu\}$ is the vector of nodal-point electrical potentials, $\{Q\}$ the vector of electrical charges, $[K_{uu}]$ replaces $[K_s]$, $[M_{uu}]$ replaces $[M_s]$, $[K'_{\nu\nu}]$ is the piezoelectric stiffness matrix, and $[K'_{u\nu}]$ and $[K'_{\nu u}]$ are the electro-elastic coupling matrices.

Equation (21) can now be used to predict the in-air response of the free-flooded cylinder transducer by calculating the resonance (short circuit) and antiresonance (open circuit) frequencies and electrical capacitance.

The electrical-potential degrees of freedom must first be condensed to one degree of freedom by applying the appropriate boundary conditions. This one electrical-potential degree of freedom is the potential which is applied across the transducer's input terminals. The potential degrees of freedom for the nodal points on one side of a stave of the cylinder are all set equal to the driving potential ν_0, and the potential degrees of freedom on the opposite side of the stave are all set to zero. These two sides are the silvered surfaces (see Fig. 1) to which the driven and grounded input terminals are attached. The remaining potential degrees of freedom in the stave's interior are left free. The application of these boundary conditions and a repartitioning makes it possible to write Eq. (21) in the form

$$\left[\begin{array}{c|c} M_{1,1} & 0 \\ \hline 0 & 0 \end{array}\right] \begin{Bmatrix} \ddot{u} \\ \ddot{\nu}_0 \\ \hline \ddot{\nu} \end{Bmatrix} + \left[\begin{array}{c|cc} K_{1,1} & K_{1,2} \\ \hline K_{2,1} & K_{2,2} \end{array}\right] \begin{Bmatrix} u \\ \nu_0 \\ \hline \nu \end{Bmatrix} = \begin{Bmatrix} 0 \\ Q \\ \hline 0 \end{Bmatrix} . \tag{22}$$

The second equation of Eq. (22) can be written as

$$[K_{2,1}] \begin{Bmatrix} u \\ \nu_0 \end{Bmatrix} + [K_{2,2}] \{\nu\} = \{0\} ,$$

or

$$\{\nu\} = - [K_{2,2}]^{-1} [K_{2,1}] \begin{Bmatrix} u \\ \nu_0 \end{Bmatrix} . \tag{23}$$

Substituting Eq. (23) into the first equation of Eq. (22) yields

$$[M_{1,1}] \begin{Bmatrix} \ddot{u} \\ \ddot{\nu}_0 \end{Bmatrix} + [K_{1,1}] \begin{Bmatrix} u \\ \nu_0 \end{Bmatrix} - [K_{1,2}] [K_{2,2}]^{-1} [K_{2,1}] \begin{Bmatrix} u \\ \nu_0 \end{Bmatrix} = \begin{Bmatrix} 0 \\ Q \end{Bmatrix} ,$$

or

$$[M_{1,1}] \begin{Bmatrix} \ddot{u} \\ \ddot{v}_0 \end{Bmatrix} + [\bar{K}_{1,1}] \begin{Bmatrix} u \\ v_0 \end{Bmatrix} = \begin{Bmatrix} 0 \\ Q \end{Bmatrix} , \tag{24}$$

where

$$[\bar{K}_{1,1}] \equiv [K_{1,1}] - [K_{1,2}] [K_{2,2}]^{-1} [K_{2,1}] . \tag{25}$$

Equation (24) can itself be written in the partitioned form

$$\begin{bmatrix} M_{uu} & 0 \\ 0 & 0 \end{bmatrix} \begin{Bmatrix} \ddot{u} \\ \ddot{v}_0 \end{Bmatrix} + \begin{bmatrix} K_{uu} & K_{uv} \\ K_{vu} & K_{vv} \end{bmatrix} \begin{Bmatrix} u \\ v_0 \end{Bmatrix} = \begin{Bmatrix} 0 \\ Q \end{Bmatrix} . \tag{26}$$

A resonance of the piezoelectric-ceramic cylinder occurs when the difference in the electrical potentials applied to the silvered surfaces of each stave is zero. Therefore, with $v_0 = 0$, Eq. (26) reduces to

$$[-\omega_R^2 M_{uu} + K_{uu}] \{u_R\} = \{0\} \tag{27}$$

if a harmonic time dependence is assumed. The resonance frequencies and their associated modeshapes can now be found. This is sometimes referred to as the short-circuit case.

An antiresonance of the cylinder occurs when the current to the transducer is zero. Therefore, with $Q = 0$, the last equation of Eq. (26) can be written as

$$\langle K_{vu} \rangle \{u\} + K_{vv} v_0 = 0 ,$$

or

$$v_0 = - \frac{\langle K_{vu} \rangle}{K_{vv}} \{u\} . \tag{28}$$

Substituting Eq. (28) into the first equation of Eq. (26) yields

$$[M_{uu}] \{\ddot{u}\} + [\bar{K}_{uu}] \{u\} = \{0\} , \tag{29}$$

where

$$[\bar{K}_{uu}] \equiv [K_{uu}] - [K_{uv}] \frac{\langle K_{vu} \rangle}{K_{vv}} . \tag{30}$$

Again, assuming a harmonic time dependence, Eq. (29) becomes

$$[-\omega_A^2 \, M_{uu} + \bar{K}_{uu}] \, \{u_A\} = \{0\} \, , \tag{31}$$

and the antiresonance frequencies and their associated modeshapes can now be found. This is the open-circuit case.

For a free-flooded cylinder, three resonant modes of vibration are of interest: the breathing, the bending, and the length modes. Fig. 3 shows these three modes in a cross-sectional display of the cylinder. The breathing mode is the best radiator of sound and is strongly excited in air. The bending mode is weakly coupled to the electrical drive and is weakly excited in air. The length mode is a poor radiator of sound because of the small volume displacements involved. When the cylinder is placed in water, however, combinations of the free-vibrational modes of the cylinder may become excited because of the acoustic radiation coupling.

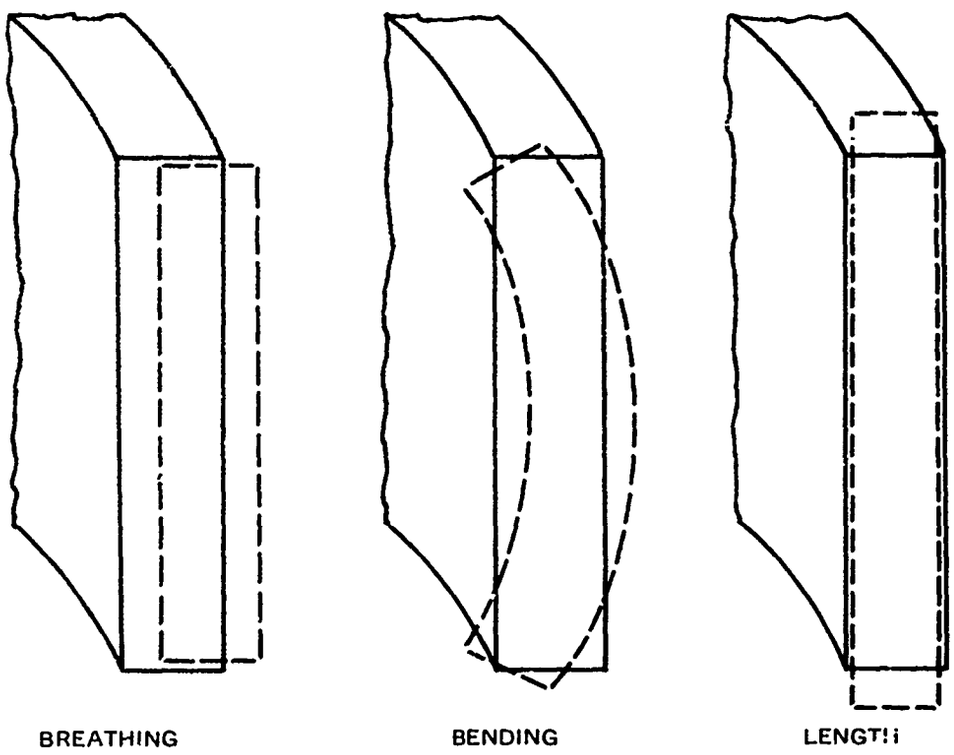

Figure 3. Cross-sectional drawing of the first three resonant modes of a free-flooded cylinder.

The electrical capacitance at a circular frequency ω_c can be calculated by rewriting Eq. (26) in the form

$$\begin{bmatrix} K_{uu} - \omega_c^2 M_{uu} & K_{u\nu} \\ K_{\nu u} & K_{\nu\nu} \end{bmatrix} \begin{Bmatrix} u \\ \nu_0 \end{Bmatrix} = \begin{Bmatrix} 0 \\ Q \end{Bmatrix} . \tag{32}$$

Solving the first equation of Eq. (32) for {u} yields

$$\{u\} = - [K_{uu} - \omega^2 M_{uu}]^{-1} \{K_{u\nu}\} \nu_0 . \tag{33}$$

Substituting Eq. (33) into the latest equation of Eq. (32) results in

$$\left(\langle K_{\nu u} \rangle [K_{uu} - \omega_c^2 M_{uu}]^{-1} \{K_{uv}\} + K_{\nu\nu} \right) \nu_0 = Q , \tag{34}$$

or

$$C\nu_0 = Q ,$$

where the capacitance C is defined by

$$C \equiv K_{\nu\nu} - \langle K_{\nu u} \rangle [K_{uu} - \omega_c^2 M_{uu}]^{-1} \{K_{u\nu}\} . \tag{35}$$

IN-WATER RESPONSE

If the in-air results calculated by means of Eqs. (27), (31) and (35) are as desired, then this finite-element mathematical model for the free-flooded cylinder transducer can now be combined in a mathematical model of the transducer immersed in an infinite fluid medium; i.e., the in-water, free-field response of the transducer can now be calculated.

Equations (20) and (26) can be combined into one matrix equation of the form

$$\begin{bmatrix} M_f & \rho T^T & 0 \\ 0 & M_{uu} & 0 \\ 0 & 0 & 0 \end{bmatrix} \begin{Bmatrix} \ddot{p} \\ \ddot{u} \\ \ddot{\nu}_0 \end{Bmatrix} + \begin{bmatrix} K_f & 0 & 0 \\ -T & K_{uu} & K_{u\nu} \\ 0 & K_{\nu u} & K_{\nu\nu} \end{bmatrix} \begin{Bmatrix} p \\ u \\ \nu \end{Bmatrix} = \begin{Bmatrix} F_f \\ 0 \\ Q \end{Bmatrix} . \tag{36}$$

The nodal-point forces F_f acting on the surface S_1 arise from the presence of the exterior infinite acoustic fluid of region R_2. To obtain an expression for this forcing function, the surface Helmholtz integral equation can be used (Refs. 20-22). This can be considered as the boundary condition that is applied to surface S_1 because of the interaction between region R_1 and region R_2. The integral formulation relates the acoustic pressure p at any point x in the region R_2 to the integral of the acoustic pressure and its normal

derivative over the closed surface S_1. The surface Helmholtz integral equation can be written in the form

$$p(x) = \frac{1}{4\pi} \int_{S_1} \left\{ p(\xi) \frac{\partial}{\partial n_\xi} \left[\frac{e^{-jkd(x,\xi)}}{d(x,\xi)} \right] - \frac{\partial p(\xi)}{\partial n_\xi} \left[\frac{e^{-jkd(x,\xi)}}{d(x,\xi)} \right] \right\} dS(\xi) \quad , \tag{37}$$

where k is the wave number ω/c (ω the circular frequency and c the speed of sound in the fluid), and the pressure in region R_2 must satisfy the radiation condition on a spherical surface S_R at infinity (Ref. 21); i.e.,

$$\lim_{R\to\infty} \int_{S_R} \left| \frac{\partial p(r)}{\partial r} + jkp(r) \right|^2_{r=R} dS = 0 \quad . \tag{38}$$

The relationship between the pressure field and its normal derivative on the surface S_1 can be calculated in several ways (Refs. 12, 23 and 24). However, since the surface S_1 has been chosen to be spherical, the steady-state acoustic-radiation Green's function separates when expanded in spherical harmonics (Ref. 25), and the radiation impedance associated with each spherical harmonic subspace can be obtained in an analytical form. This avoids the costly numerical evaluation of numerous integrals, such as is performed in the formulation given in Ref. 11. By expanding the pressures and normal velocities at the finite-element nodal points on surface S_1 in a finite spherical harmonic series, it is possible to derive an analytical solution for the radiation impedance on S_1. Reference 13 gives the details of this calculation. Writing Eq. (11) as

$$\frac{\partial p(\xi)}{\partial n_\xi} = -j\omega\rho v^n(\xi) \quad , \tag{39}$$

the relationship between the coefficients of a spherical harmonic expansion of the pressure and the coefficients of normal velocity on the spherical surface S_1 of radius a can be written as

$$v^n_\ell(a) = \frac{1}{j\omega\rho a} \frac{1}{\lambda_\ell(ka)} p_\ell(a) \quad . \tag{40}$$

The radiation admittance $1/\lambda_\ell(ka)$ is defined in Appendix A of Ref. 13 as

$$1/\lambda_\ell(ka) \equiv \ell + 1 - ka \frac{h^{(-)}_{\ell-1}(ka)}{h^{(-)}_\ell(ka)} \quad , \tag{41}$$

where $h_\ell^{(-)}(ka)$ is the ℓ^{th} order spherical Hankel function (Ref. 26). The expansion coefficients $p_\ell(a)$ and $v_\ell^n(a)$ are the ℓ^{th} components of the surface pressure and normal velocity, respectively, and are given by

$$p(a,\theta,\phi) = \sum_{\ell=0}^{\infty} p_\ell(a) Y_\ell^0(\theta,\phi) \quad , \tag{42}$$

and

$$v^n(a,\theta,\phi) = \sum_{\ell=0}^{\infty} v_\ell^n(a) Y_\ell^0(\theta,\phi) \quad , \tag{43}$$

with

$$p_\ell(a) = \int_0^{2\pi} d\phi \int_0^{\pi} p(a,\theta,\phi) Y_\ell^0(\theta,\phi) \sin(\theta)\, d\theta \quad , \tag{44}$$

and

$$v_\ell^n(a) = \int_0^{2\pi} d\phi \int_0^{\pi} v^n(a,\theta,\phi) Y_\ell^0(\theta,\phi) \sin(\theta)\, d\theta \quad , \tag{45}$$

where (a,θ,ϕ) are the spherical coordinates of the point ξ on S_1.

In practice, the summations in Eqs. (42) and (43) are carried out over only the first few terms. The exact number of terms that is necessary can be found by first calculating the maximum value of ka and then finding the maximum value of ℓ for which the imaginary part of the acoustic admittance is zero below this ka value. Figure 4 is a graph of the greatest value of ka versus the greatest value of ℓ. For example, for a cylinder to be operated to a maximum frequency of 20 kHz and enclosed in a fluid sphere 0.1 m in radius, the greatest value of $ka = \frac{2\pi fa}{c}$ is less than ten. From Fig. 4, the greatest value of ℓ (denoted by $\mathcal{L}$) is therefore fourteen. However, only the even-order terms need be retained because the orientation and electric drive configuration of the cylinder produce an even symmetry plane at $\theta = 90$ deg. Therefore, only those spherical harmonics which are even functions under a reflection through this symmetry plane are retained. The summations for the above example contain only eight terms.

The form of the forces acting on the fluid-sphere surface S_1 is the same as that of the forces due to the presence of the vibrating cylinder that act on the acoustic fluid [Eq. (17)], except that the coupling matrix now couples the infinite acoustic fluid exterior region to the acoustic fluid sphere via the surface-fluid finite-element interfaces. This coupling matrix will be denoted by $[M_S]$ since its elements are analogous to a consistent mass matrix; e.g., they are the integrals of a quadratic form of the interpolation function N_i over the closed

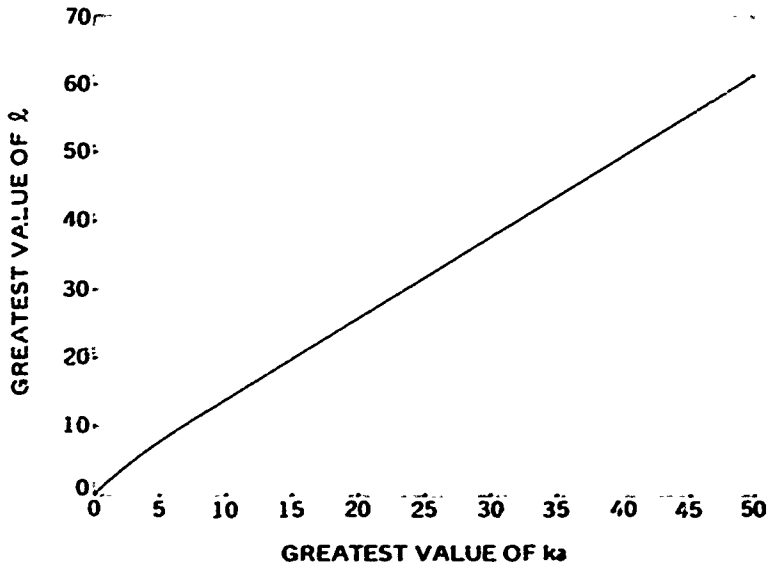

Figure 4. Plot of the greatest value of ℓ that is needed in the spherical harmonic expansion as a function of the non-dimensional frequency ka.

spherical surface S_1. The elements of the coupling matrix are defined by

$$(M_S)_{i,j} \equiv \sum_{\substack{\text{surface} \\ \text{elements}}} \int_{S_1} N_i^T N_j \, dS \quad . \tag{46}$$

The vector $\{F_f\}$ therefore has non-zero elements for those degrees of freedom associated with the finite-element nodal points that lie on the surface S_1. Partitioning Eq. (36) into a form where the surface and interior degrees of freedom are separated, the partitioned matrix equations become

$$\begin{bmatrix} (M_f)_{s,s} & 0 & (M_f)_{s,i} & (\rho T)_s^T \\ 0 & 0 & 0 & 0 \\ (M_f)_{i,s} & 0 & (M_f)_{i,i} & (\rho T)_i^T \\ 0 & 0 & 0 & M_{uu} \end{bmatrix} \begin{Bmatrix} \ddot{p}_s \\ \ddot{\nu} \\ \ddot{p}_i \\ \ddot{u} \end{Bmatrix} + \begin{bmatrix} (K_f)_{s,s} & 0 & (K_f)_{s,i} & 0 \\ 0 & K_{\nu\nu} & 0 & K_{\nu u} \\ (K_f)_{i,s} & 0 & (K_f)_{i,i} & 0 \\ -T_s & K_{uu} & -T_i & K_{uu} \end{bmatrix} \begin{Bmatrix} p_s \\ \nu \\ p_i \\ u \end{Bmatrix} = \begin{Bmatrix} F_s \\ Q \\ 0 \\ 0 \end{Bmatrix} \quad . \tag{47}$$

where

$$\{F_S\} = -\rho[M_S]\ \{\dot{v}^n\} \quad . \tag{48}$$

The vector $\{\dot{v}^n\}$ contains the accelerations defined by $\frac{\partial v^n}{\partial t}$ for each nodal point on S_I.

The subset of spherical harmonics that has been chosen must now be normalized to be compatible with the finite-element idealization of surface S_I. The normalized spherical harmonics that are the elements of the linear transformation matrix [L] are given by

$$L_\ell(\theta_i) = \frac{2\sqrt{\pi}}{a}\, Y_\ell^0(\theta_i) \quad , \tag{49}$$

and the full transformation matrix appears in the form

$$[L] = \begin{bmatrix} L_0(0) & L_2(0) & L_4(0) & \cdots & L_\ell(0) \\ \vdots & \vdots & \vdots & & \vdots \\ L_0(\theta_i) & L_2(\theta_i) & L_4(\theta_i) & \cdots & L_\ell(\theta_i) \\ \vdots & \vdots & \vdots & & \vdots \\ L_0(\pi/2) & L_2(\pi/2) & L_4(\pi/2) & \cdots & L_\ell(\pi/2) \end{bmatrix} . \tag{50}$$

The transformation matrix has been normalized such that

$$[L]^T [M_S]\ [L] = [I] \quad , \tag{51}$$

where [I] is the identity matrix.

To transform the equations for surface S_I to the chosen subset of normalized spherical harmonic basis vectors, the right-hand side of Eq. (47) is multiplied by a transformation matrix such that

$$\begin{bmatrix} L^T & 0 & 0 & 0 \\ 0 & 1 & 0 & 0 \\ 0 & 0 & 1 & 0 \\ 0 & 0 & 0 & \ddots \end{bmatrix} \text{R.H.S.} = \begin{Bmatrix} -\rho[L]^T [M_S]\ \{\dot{v}^n\} \\ Q \\ 0 \\ 0 \end{Bmatrix} \quad . \tag{52}$$

The spherical harmonic expansion of the derivatives of the nodal-point velocities can be written in the matrix form

$$\{\dot{v}^n\} = [L]\ \{\dot{v}_\ell^n\} \quad . \tag{53}$$

Using Eqs. (51) and (53), Eq. (52) becomes

$$\begin{bmatrix} L^T & 0 & 0 & 0 \\ 0 & 1 & 0 & 0 \\ 0 & 0 & 1 & 0 \\ 0 & 0 & 0 & 1 \end{bmatrix} \quad \text{R.H.S.} = \begin{Bmatrix} -\rho \dot{v}^n_\ell \\ Q \\ 0 \\ 0 \end{Bmatrix} \quad . \tag{54}$$

Substituting Eq. (40) for the normal velocity components in Eq. (54) yields

$$\begin{bmatrix} L^T & 0 & 0 & 0 \\ 0 & 1 & 0 & 0 \\ 0 & 0 & 1 & 0 \\ 0 & 0 & 0 & 1 \end{bmatrix} \quad \text{R.H.S.} = \begin{Bmatrix} -1/a\,[1/\gamma_\ell]_{\text{Diag}}\,\dot{p}_\ell \\ Q \\ 0 \\ 0 \end{Bmatrix} \quad . \tag{55}$$

Similarly, the left-hand side of Eq. (47) can be multiplied by the transformation matrix and the surface pressures expanded in spherical harmonics.

$$\{p\}_s = [L]\ \{p_\ell\} \quad . \tag{56}$$

such that

$$\begin{bmatrix} L^T & 0 & 0 & 0 \\ 0 & 1 & 0 & 0 \\ 0 & 0 & 1 & 0 \\ 0 & 0 & 0 & 1 \end{bmatrix} \text{L.H.S.} = \begin{bmatrix} L^T(M_f)_{s,s}L & 0 & L^T(M_f)_{s,i} & L^T(\rho T)_s^T \\ 0 & 0 & 0 & 0 \\ (M_f)_{i,s}L & 0 & (M_f)_{i,i} & (\rho T)_i^T \\ 0 & 0 & 0 & M_{uu} \end{bmatrix} \begin{Bmatrix} \ddot{p}_\ell \\ \ddot{v} \\ \ddot{p}_i \\ \ddot{u} \end{Bmatrix}$$

$$+ \begin{bmatrix} L^T(K_f)_{s,s}L & 0 & L^T(K_f)_{s,i} & 0 \\ 0 & K_{vv} & 0 & K_{vu} \\ (K_f)_{i,s}L & 0 & (K_f)_{i,i} & 0 \\ -T_sL & K_{uv} & -T_i & K_{uu} \end{bmatrix} \begin{Bmatrix} p_\ell \\ v \\ p_i \\ u \end{Bmatrix} \quad . \tag{57}$$

Combining Eqs. (55) and (57), the transformation of Eq. (47) can now be expressed as

$$\left[\begin{array}{cc:cc} L^T(M_f)_{s,s}L & 0 & L^T(M_f)_{s,i} & L^T(\rho T)_s^T \\ 0 & 0 & 0 & 0 \\ \hdashline (M_f)_{i,s}L & 0 & (M_f)_{i,i} & (\rho T)_i^T \\ 0 & 0 & 0 & M_{uu} \end{array}\right] \left\{\begin{array}{c} \ddot{p}_\ell \\ \ddot{\nu} \\ \ddot{p}_i \\ \ddot{u} \end{array}\right\}$$

$$+ \left[\begin{array}{cc:cc} L^T(K_f)_{s,s}L + 1/a(1/\gamma_\ell)_{Diag} & 0 & L^T(K_f)_{s,i} & 0 \\ 0 & K_{\nu\nu} & 0 & K_{\nu u} \\ \hdashline (K_f)_{i,s}L & 0 & (K_f)_{i,i} & 0 \\ -T_s L & K_{uv} & -T_i & K_{uu} \end{array}\right] \left\{\begin{array}{c} p_\ell \\ \nu \\ p_i \\ u \end{array}\right\} = \left\{\begin{array}{c} 0 \\ Q \\ 0 \\ 0 \end{array}\right\} . \quad (58)$$

Equation (58) can be solved at a set of circular driving frequencies ω for the unknown field variables p_ℓ, ν, p_i and u in terms of the known electrical forcing function Q. However, this is a large system of equations, and a total solution at each frequency would be costly. Typically, the equations are more than one hundred fifty in number. To reduce the number of equations that need to be solved at each frequency, Eq. (58) is partitioned as shown above. The second set of equations of Eq. (58) can be solved for

$$\left\{\begin{array}{c} p_i \\ u \end{array}\right\}$$

and the solution substituted into the first set of equations. Partitioning the matrices such that the interior problem (Refs. 12 and 20) can be solved separately yields a small system of surface equations to be solved at each driving frequency. If the driving frequency is near an eigenfrequency of the interior problem, then the surface equations are overdetermined by one degree of freedom. That one degree of freedom is the eigenvector of the interior problem that is associated with that eigenfrequency.

To calculate the interior eigenvalues and eigenvectors, the lower right-hand blocks of Eq. (58) can be written separately. However, a simple modification, suggested by O. C. Zienkiewicz and B. M. Irons (Ref. 17), produces a symmetric form for the equations describing the interior problem which makes it easier and less expensive to calculate all of the eigenvalues and eigenvectors. Solving the third equation of Eq. (58) for $\{p\}_i$ yields

$$\begin{aligned} \{p\}_i = &-[K_f]_{i,i}^{-1}[M_f]_{i,s}[L]\{\ddot{p}_\ell\} - [K_f]_{i,i}^{-1}[M_f]_{i,i}\{\ddot{p}\}_i \\ &-[K_f]_{i,i}^{-1}[\rho T]_i^T\{\ddot{u}\} - [K_f]_{i,i}^{-1}[K_f]_{i,s}[L]\{p_\ell\} . \end{aligned} \quad (59)$$

Substituting this expression for $\{p\}_i$ into the fourth equation of Eq. (58) yields

$$
\begin{aligned}
&[T]_i\,[K_f]_{i,i}^{-1}\,[M_f]_{i,s}\,[L]\,\{\ddot{p}_\ell\} + [T]_i\,[K_f]_{i,i}^{-1}\,[M_f]_{i,i}\,\{\ddot{p}\}_i \\
&\quad + ([M_{uu}] + [T]_i\,[K_f]_{i,i}^{-1}\,[\rho T]_i^T)\,\{\ddot{u}\} \\
&\quad + (-[T_s]\,[L] + [T]_i\,[K_f]_{i,i}^{-1}\,[K_f]_{i,s}\,[L])\,\{p_\ell\} \\
&\quad + \{K_{uv}\}\,\nu + [K_{uu}]\,\{u\} = \{0\}\,. \qquad (60)
\end{aligned}
$$

Multiplying Eq. (59) by $[M_f]_{i,i}$ and Eq. (60) by ρ and substituting them for the third and fourth equations of Eq. (58) results in

$$
\left[\begin{array}{cc:cc}
L^T (M_f)_{s,s} L & 0 & L^T (M_f)_{s,i} & L^T (\rho T)_s^T \\
0 & 0 & 0 & 0 \\
\hdashline
(M_f)_{i,i} (K_f)_{i,i}^{-1} (M_f)_{i,s} L & 0 & (M_f)_{i,i} (K_f)_{i,i}^{-1} (M_f)_{i,i} & (M_f)_{i,i} (K_f)_{i,i}^{-1} (\rho T)_i^T \\
(\rho T)_i (K_f)_{i,i}^{-1} (M_f)_{i,s} L & 0 & (\rho T)_i (K_f)_{i,i}^{-1} (M_f)_{i,i} & \rho M_{uu} + (\rho T)_i (K_f)_{i,i}^{-1} (\rho T)_i^T
\end{array}\right]
\left\{\begin{array}{c} \ddot{p}_\ell \\ \ddot{\nu} \\ \hdashline \ddot{p}_i \\ \ddot{u} \end{array}\right\}
$$

$$
+ \left[\begin{array}{cc:cc}
L^T (K_f)_{s,s} L + 1/a\,(1/\gamma_\ell)_{Diag} & 0 & L^T (K_f)_{s,i} & 0 \\
0 & K_{vv} & 0 & K_{vu} \\
\hdashline
(M_f)_{i,s} (K_f)_{i,i}^{-1} (K_f)_{i,s} L & 0 & (M_f)_{i,i} & 0 \\
-(\rho T)_s L + (\rho T)_i (K_f)_{i,i}^{-1} (K_f)_{i,s} L & \rho K_{uv} & 0 & \rho K_{uu}
\end{array}\right]
\left\{\begin{array}{c} p_\ell \\ \nu \\ \hdashline p_i \\ u \end{array}\right\}
= \left\{\begin{array}{c} 0 \\ Q \\ \hdashline 0 \\ 0 \end{array}\right\} \qquad (61)
$$

The lower right-hand blocks of Eq. (61) are now symmetric matrices and can be considered as a matrix equation of the form

$$
\left[\begin{array}{cc}
(M_f)_{i,i} (K_f)_{i,i}^{-1} (M_f)_{i,i} & (M_f)_{i,i} (K_f)_{i,i}^{-1} (\rho T)_i^T \\
(\rho T)_i (K_f)_{i,i}^{-1} (M_f)_{i,i} & \rho M_{uu} + (\rho T)_i (K_f)_{i,i}^{-1} (\rho T)_i^T
\end{array}\right]
\left\{\begin{array}{c} \ddot{p}_i \\ \ddot{u} \end{array}\right\}
$$

$$
+ \left[\begin{array}{cc}
(M_f)_{i,i} & 0 \\
0 & \rho K_{uu}
\end{array}\right]
\left\{\begin{array}{c} p_i \\ u \end{array}\right\}
= \left\{\begin{array}{c} 0 \\ 0 \end{array}\right\} \quad . \qquad (62)
$$

These are the equations of motion for the free vibrations of the coupled structure/acoustic-fluid-sphere problem with the boundary condition of zero pressure on the sphere surface

(the Dirichlet boundary condition). The eigenvectors of this system form a square transformation matrix [U] such that the first column of the matrix is the eigenvector that corresponds to the smallest eigenvalue. Operating with this transformation on the "mass" and "stiffness" matrices of Eq. (62) results in

$$[U]^T \begin{bmatrix} (M_f)_{i,i}\,(K_f)^{-1}_{i,i}\,(M_f)_{i,i} & (M_f)_{i,i}\,(K_f)^{-1}_{i,i}\,(\rho T)^T_i \\ (\rho T)_i\,(K_f)^{-1}_{i,i}\,(M_f)_{i,i} & \rho M_{uu} + (\rho T)_i\,(K_f)^{-1}_{i,i}\,(\rho T)^T_i \end{bmatrix} [U] = [I_n] \quad , \tag{63}$$

and

$$[U]^T \begin{bmatrix} (M_f)_{i,i} & 0 \\ 0 & \rho K_{uu} \end{bmatrix} [U] = \begin{bmatrix} \omega_1^2 & 0_2 & \cdots & 0 \\ 0 & \omega_2 & \cdots & 0 \\ \vdots & \vdots & \ddots & \vdots \\ 0 & 0 & \cdots & \omega_n^2 \end{bmatrix} = [\omega_n^2]_{Diag.} \tag{64}$$

Applying the transformation [U] to Eq. (61) and expanding $\begin{Bmatrix} p_i \\ u \end{Bmatrix}$ such that

$$\begin{Bmatrix} p_i \\ u \end{Bmatrix} = [U]\,\{g\} \quad , \tag{65}$$

where {g} is the set of unknown coefficients of an expansion in the eigenvector basis functions, yields a set of equations of the form

$$\left[\begin{array}{c|c} M_{1,1} & M_{1,2} \\ \hline M_{2,1} & I_n \end{array}\right] \begin{Bmatrix} \ddot{p}_\ell \\ \ddot{\nu} \\ \hline \ddot{g} \end{Bmatrix} + \left[\begin{array}{c|c} K_{1,1} & K_{1,2} \\ \hline K_{2,1} & (\omega_n^2)_{Diag} \end{array}\right] \begin{Bmatrix} p_\ell \\ \nu \\ \hline g \end{Bmatrix} = \begin{Bmatrix} 0 \\ Q \\ \hline 0 \end{Bmatrix} \quad . \tag{66}$$

if the following definitions are made:

$$[M_{1,1}] \equiv \begin{bmatrix} L^T (M_f)_{s,s}\, L & 0 \\ 0 & 0 \end{bmatrix} \quad ,$$

$$[M_{1,2}] \equiv \begin{bmatrix} L^T (M_f)_{s,i} & L^T (\rho T)^T_s \\ 0 & 0 \end{bmatrix} [U] \quad , \tag{67}$$

$$[M_{2,1}] \equiv [U]^T \begin{bmatrix} (M_f)_{i,i}\,(K_f)^{-1}_{i,j}\,(M_f)_{i,s}\, L & 0 \\ (\rho T)_i\,(K_f)^{-1}_{i,i}\,(M_f)_{i,s}\, L & 0 \end{bmatrix} \quad ,$$

$$[K_{1,1}] \equiv \begin{bmatrix} L^T (K_f)_{s,s} L + (1/\gamma_\ell)_{Diag} & 0 \\ 0 & K_{\nu\nu} \end{bmatrix} ,$$

$$[K_{1,2}] \equiv \begin{bmatrix} L^T (K_f)_{s,i} & 0 \\ 0 & K_{\nu u} \end{bmatrix} [U] ,$$

and

$$[K_{2,1}] \equiv [U]^T \begin{bmatrix} (M_f)_{i,i} (K_f)^{-1}_{i,i} (K_f)_{i,s} L & 0 \\ -(\rho T)_s L + (\rho T)_i (K_f)^{-1}_{i,i} (K_f)_{i,s} L & \rho K_{uv} \end{bmatrix} .$$

Equation (66) can be solved in the frequency domain by first solving the second set of equations for {g} and substituting the solution into the first set of equations. For driving frequencies that are close to an interior eigenfrequency, a solution to the first set of equations cannot be found because factors of $1/(\omega_i^2 - \omega^2)$ are present. To avoid this singularity problem, the transformed surface pressure and electric potential equations are augmented by the eigenvector that is associated with the interior eigenfrequency that is close to the driving frequency. Therefore, the system of equations never needs to be overdetermined by more than one equation. However, for convenience, all those equations that are associated with eigenfrequencies of the interior problem that lie inside the frequency band of interest can as a block be used to augment the surface equations; i.e., $[K_{1,1}]$ and $[M_{1,1}]$ are enlarged by k rows and columns. Equation (66) now appears as

$$\left[\begin{array}{c:c} \bar{M}_{1,1} & \bar{M}_{1,2} \\ \hdashline \bar{M}_{2,1} & I_{n-k} \end{array}\right] \begin{Bmatrix} \ddot{p}_\ell \\ \ddot{\nu} \\ \ddot{g}_k \\ \hdashline \ddot{g}_{n-k} \end{Bmatrix} + \left[\begin{array}{c:c} \bar{K}_{1,1} & \bar{K}_{1,2} \\ \hdashline \bar{K}_{2,1} & (\omega^2_{n-k})_{Diag} \end{array}\right] \begin{Bmatrix} p_\ell \\ \nu \\ g_k \\ \hdashline g_{n-k} \end{Bmatrix} = \begin{Bmatrix} 0 \\ Q \\ 0 \\ \hdashline 0 \end{Bmatrix} , \qquad (68)$$

if the following definitions are made:

$$[\bar{M}_{1,1}] \equiv \begin{bmatrix} M_{1,1} & (M_{1,2})_k \\ (M_{2,1})_k & I_k \end{bmatrix} , \qquad (69a)$$

$$[\bar{M}_{1,2}] \equiv \begin{bmatrix} (M_{1,2})_{n-k} \\ 0 \end{bmatrix} , \qquad (69b)$$

$$[\bar{M}_{2,1}] \equiv [(M_{2,1})_{n-k} \quad 0] , \qquad (69c)$$

$$[\bar{K}_{1,1}] \equiv \begin{bmatrix} K_{1,1} & (K_{1,2})_k \\ (K_{2,1})_k & (\omega_k^2)_{Diag} \end{bmatrix} , \tag{69d}$$

$$[\bar{K}_{1,2}] \equiv \begin{bmatrix} (K_{1,2})_{n-k} \\ 0 \end{bmatrix} , \tag{69e}$$

and

$$[\bar{K}_{2,1}] \equiv [(K_{2,1})_{n-k} \quad 0] . \tag{69f}$$

The subscripts k and n-k refer to the blocks of the matrices that are associated with the k smallest and n-k largest (the remainder out of n total) interior eigenvalues. The value of k is associated with the lowest eigenfrequency that lies above the frequency band of interest.

Assuming a time dependence of $e^{j\omega t}$, the second equation of Eq. (68) can be solved for

$$\{g_{n-k}\} = \left[\frac{1}{\omega_{n-k}^2 - \omega^2}\right]_{Diag} [\omega^2 \bar{M}_{2,1} - \bar{K}_{2,1}] \begin{Bmatrix} p_\ell \\ \nu \\ g_k \end{Bmatrix} . \tag{70}$$

Substituting Eq. (70) into the solution to the first equation of Eq. (68) results in

$$\begin{Bmatrix} p_\ell \\ \nu \\ g_k \end{Bmatrix} = [(-\omega^2 \bar{M}_{1,1} + \bar{K}_{1,1}) + (-\omega^2 \bar{M}_{1,2} + \bar{K}_{1,2}) \left(\frac{1}{\omega_{n-k}^2 - \omega^2}\right)_{Diag} \cdot (\omega^2 M_{2,1} - K_{2,1})]^{-1} \begin{Bmatrix} 0 \\ Q \\ 0 \end{Bmatrix} . \tag{71}$$

In general, this set of equations is not large; therefore, solving the system at a great number of frequencies is not expensive.

The complex electrical impedance of the piezoelectric-ceramic cylinder can now be calculated as a function of frequency. Defining the complex impedance Z from

$$\nu = ZI , \tag{72}$$

where the current I is defined by

$$I \equiv \frac{\partial Q}{\partial t} ,$$

and

$$Q = Q_0 e^{j\omega t} \quad ,$$

the electrical-charge forcing function can be written as

$$Q = \frac{I}{j\omega} \quad . \tag{73}$$

Substituting Eqs. (72) and (73) into Eq. (71) yields

$$\begin{Bmatrix} p_\ell \\ Z \\ g_k \end{Bmatrix} = [(-\omega^2 \bar{M}_{1,1} + \bar{K}_{1,1}) + (-\omega^2 \bar{M}_{1,2} + \bar{K}_{1,2}) \left(\frac{1}{\omega_{n\text{-}k}^2 - \omega^2}\right)_{Diag} \cdot (\omega^2 M_{2,1} - K_{2,1})]^{-1} \begin{Bmatrix} 0 \\ 1/j\omega \\ 0 \end{Bmatrix} \quad . \tag{74}$$

The solution vector for Eq. (71) that is obtained for constant-voltage drive

$$\begin{Bmatrix} \bar{p}_\ell \\ 1 \\ \bar{g}_k \end{Bmatrix}$$

can be calculated from Eq. (74) by normalizing the solution to Eq. (74) to the impedance Z; i.e.,

$$\begin{Bmatrix} \bar{p}_\ell \\ 1 \\ \bar{g}_k \end{Bmatrix} = [(-\omega^2 \bar{M}_{1,1} + \bar{K}_{1,1}) + (-\omega^2 \bar{M}_{1,2} + \bar{K}_{1,2}) \left(\frac{1}{\omega_{n\text{-}k}^2 - \omega^2}\right)_{Diag} \cdot (\omega^2 \bar{M}_{2,1} - \bar{K}_{2,1})]^{-1} \begin{Bmatrix} 0 \\ 1/j\omega Z \\ 0 \end{Bmatrix} \quad . \tag{75}$$

The surface and interior acoustic-fluid-sphere pressures and the cylinder displacements per input volt can now be calculated from Eqs. (56), (65) and (70).

Since the mathematical formulation presented here includes no structural damping, the efficiency of the transducer is 100 percent. Therefore, the radiated acoustic power is equal to the electric power delivered to the transducer. The radiated power P can be calculated from

$$P = \tfrac{1}{2} \operatorname{Re} (vI^*). \tag{76}$$

Substituting Eq. (72) into Eq. (76) yields

$$P = \tfrac{1}{2} \mathrm{Re}\,(vv^{*}Z^{*}) \quad . \tag{77}$$

When $vv^{*} = 1$, Eq. (77) calculates the radiated power per input volt and can be written as

$$P = \tfrac{1}{2} \frac{\mathrm{Re}(Z)}{[Z]^{2}} \quad . \tag{78}$$

The components of a spherical harmonic expansion of the pressure at any point $x(r,\theta')$ in region R_2 are given by

$$p_{\ell}(r) = p_{\ell}(a) \frac{h_{\ell}^{(-)}(kr)}{h_{\ell}^{(-)}(ka)} \quad , \tag{79}$$

where $p_{\ell}(a)$ is given by Eq. (75). The actual pressure at x can now be calculated by using Eq. (56) for the appropriate angular coordinates; i.e.,

$$\{p(r,\theta')\} = [L(\theta')]\ \{p_{\ell}(r)\} \quad . \tag{80}$$

The derivations of these equations are found in Appendix B of Ref. 13. If the transformation matrix [L] of Eq. (56) is now used in Eq. (80), then the pressures in region R_2 are calculated at points on the surface of a sphere of radius r with the same angular distribution as the nodal points on surface S_1. The calculated vector $\{p(r,\theta')\}$ is really a vertical directivity pattern.

3 COMPUTER IMPLEMENTATION

The mathematical formulation that has been constructed for the analysis of tangentially polarized, piezoelectric-ceramic, free-flooded cylinder transducers was implemented in a series of three computer programs. The first program generates input data for the second and third programs. The second program is a MARTSAM finite-element instruction program, and it calculates the cylinder's in-air response and forms the matrices that comprise Eq. (74). The third program performs a frequency sweep, and at each frequency it calculates the complex electrical impedance, radiated power per input volt, and transmitting voltage response. Directivity patterns and cylinder displacement distributions can be calculated for selected frequencies.

PROGRAM DATFFC*

This program takes given dimensions of the cylinder to be analyzed and specified finite-element idealizations of the acoustic-fluid-sphere surface and the cylinder and generates the necessary data for the second and third programs. The computer program DATFFC needs to have the following input parameters specified by the user in MKS units:

RI, inner radius of the cylinder
RO, outer radius of the cylinder
RLNTH, total length of the cylinder
NSTAVE, number of staves that comprise the cylinder
SMALLA, radius of the fluid-sphere surface S_1
RHO, density of the acoustic fluid
RCV, speed of sound in the acoustic fluid
DENSTY, density of the piezoelectric-ceramic material
RMATPM(I), ten piezoelectric-ceramic material parameters (see Ref. 8)
NPSR, number of fluid-sphere surface elements
NLR, number of structure elements along the half-length of the cylinder
NTR, number of structure elements through the thickness of the cylinder
NSPHH, number of terms used in the spherical harmonic expansions
KAUG, number of degrees of freedom used to augment the surface equations to prevent singularities in the solution over the frequency band of interest
CAPFRQ, the frequency at which the in-air electrical capacitance of the transducer is to be calculated

The structure has midplane reflective symmetry in the z-direction and N-fold reflective and rotational symmetry about the z-axis. The structure therefore consists of N unit cells. It is necessary to mathematically model only one unit cell and apply the boundary conditions of zero azimuthal displacement for the boundaries of the unit cell that are shared by its neighboring cells. Because the electrical driving force is axisymmetric, only m = 0 circular harmonic motion is considered (see Ref. 13). This means that the cylinder displacements and the acoustic-fluid pressures are independent of the azimuthal angle ϕ, and if the displacements of the cylinder are written in terms of a cylindrical coordinate system, then all azimuthal degrees of freedom can be set to zero with no loss of accuracy over the frequency band of interest. The mathematical modeling can therefore be reduced to a two-dimensional problem even though the unit cell of the cylinder, one stave, is not axisymmetric. In addition, because the cylinder has midplane reflective symmetry (see Fig. 5), modeling of only the top half of a stave and the top half of the fluid sphere and applying the symmetry boundary condition of setting to zero the z-displacements of the cylinder in this plane is sufficient to generate the results for the entire cylinder (Ref. 27).

From the list of input parameters, the fluid sphere is idealized into FTAXI2 MARTSAM finite elements based upon the number of elements specified for the sphere

* DATFFC: from data generation program for the analysis of free-flooded cylinders.

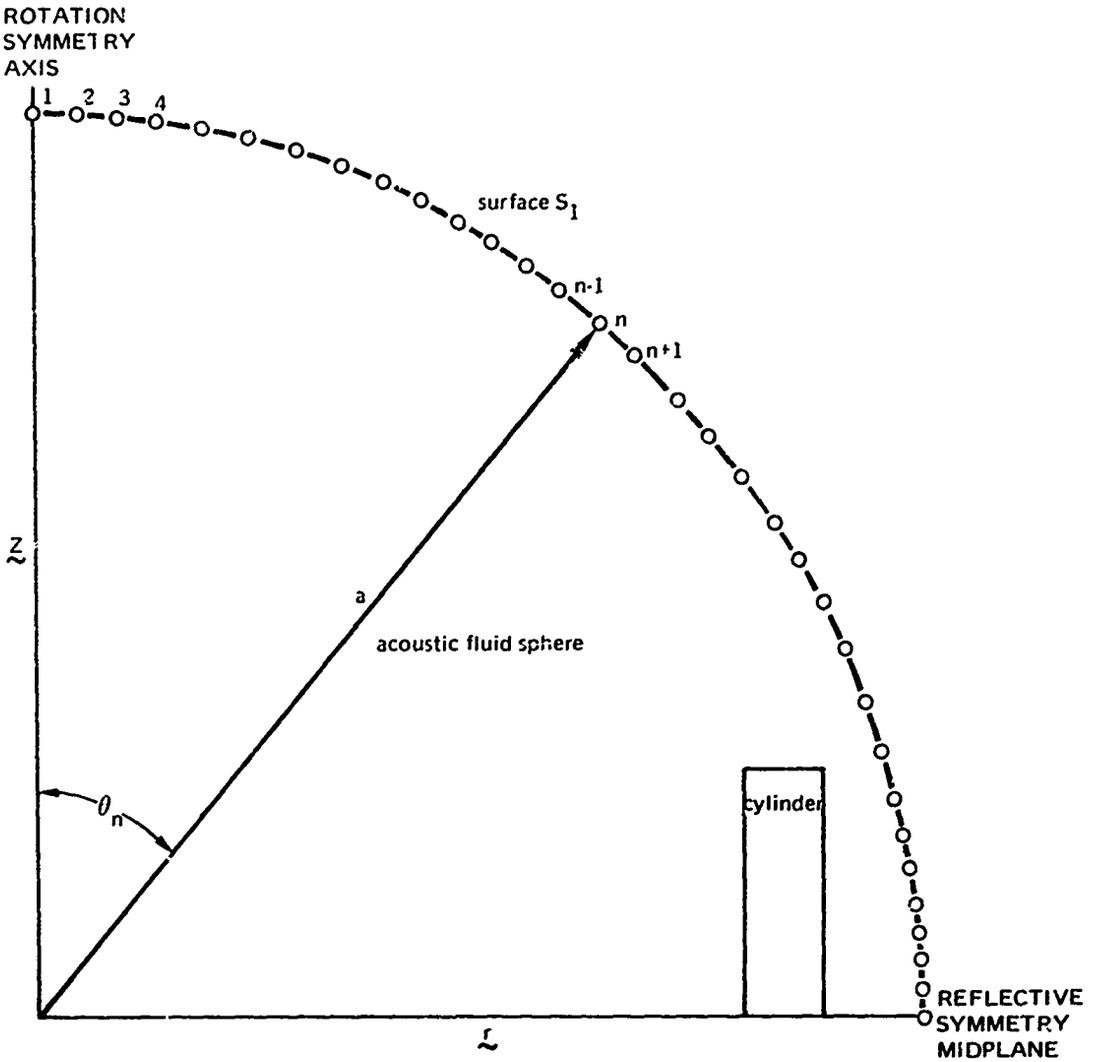

Figure 5. Cross-sectional drawing of the cylinder and fluid sphere surface showing the rotational symmetry axis and reflective symmetry midplane.

surface and the cylinder length and thickness. The FTAXI2 element is a compressible fluid axisymmetric element with a triangular cross section. Each element has six nodal points with a single degree of freedom, the pressure, associated with each node. Figure 6 shows a typical fluid-sphere idealization. The triangles are calculated by means of a triangularization routine developed for a contour plotting program (Ref. 28). Lists of the (r, z) coordinates of each nodal point in the fluid sphere idealization (COORDF) and the fluid material parameters and element assembly data (ELMNTF) are produced.

The finite-element model for the piezoelectric-ceramic cylinder is generated by modeling the top half of one stave of the cylinder with PHEX20 MARTSAM finite elements. Again, the idealization is determined from the list of input parameters. The PHEX20 element is a solid, three-dimensional element with 20 nodal points for each element. Each nodal point has three displacement degrees of freedom (x, y and z in a rectangular coordinate

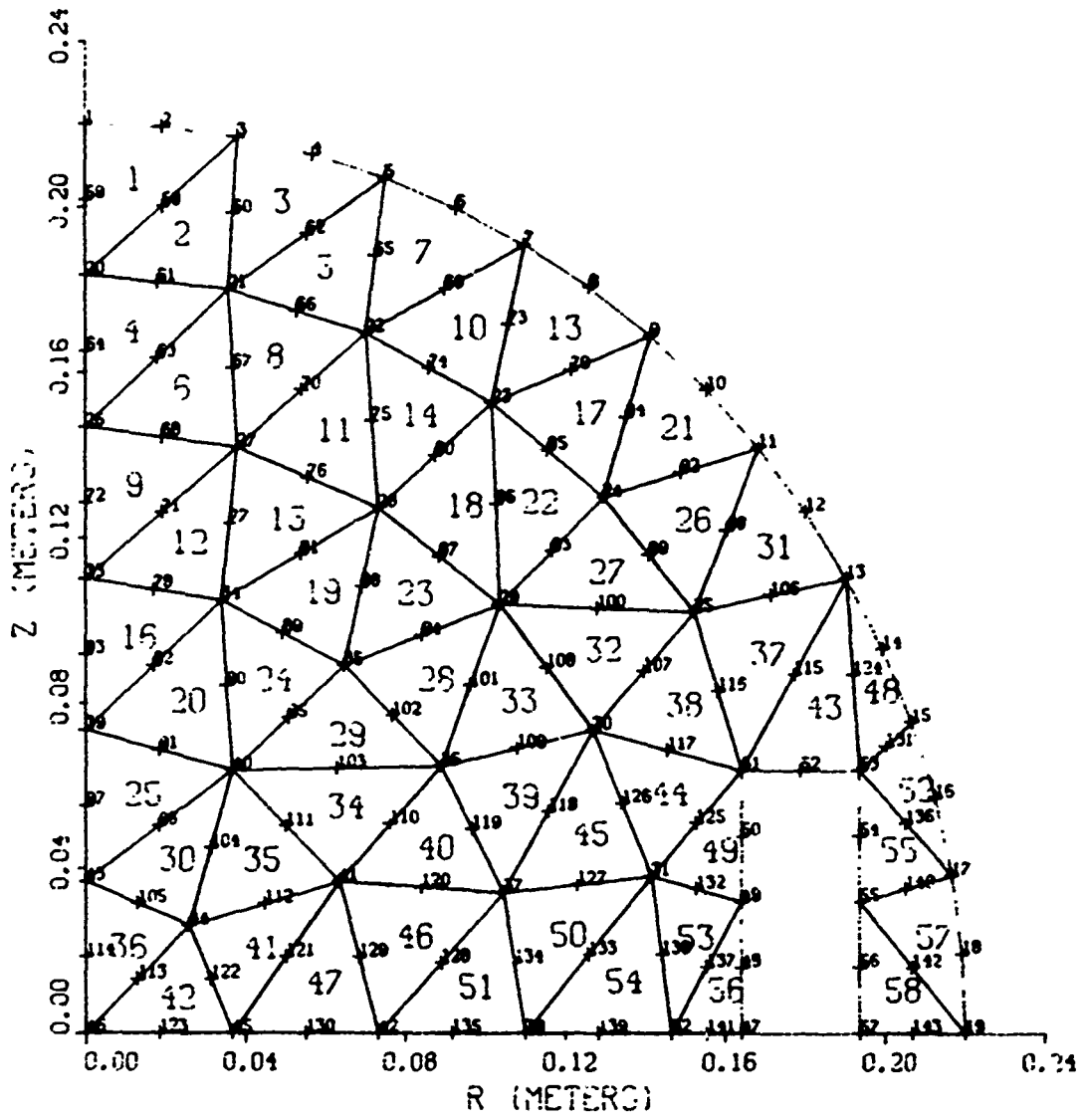

Figure 6. Cross-sectional display of the finite-element idealization of the top half of the acoustic fluid sphere that encloses the cylinder.

system) and an electrical-potential degree of freedom ν. Fig. 7 shows a typical stave idealization. Lists of the (x, y, z) coordinates of each stave nodal point (COORDS) and the piezoelectric-ceramic material parameters and stave element assembly data (ELMNTS) are calculated.

When the coordinate data COORDS and assembly data ELMNTS are used in the MARTSAM finite-element program, the mass and stiffness matrices are generated for the stave model in a rectangular coordinate system. Because an axisymmetric structural representation is desired, it is necessary to transform the equations to a cylindrical coordinate system. The DATFFC program generates a list of rotation angles for each nodal point (BCLIST), which MARTSAM can then use to perform the coordinate system transformation.

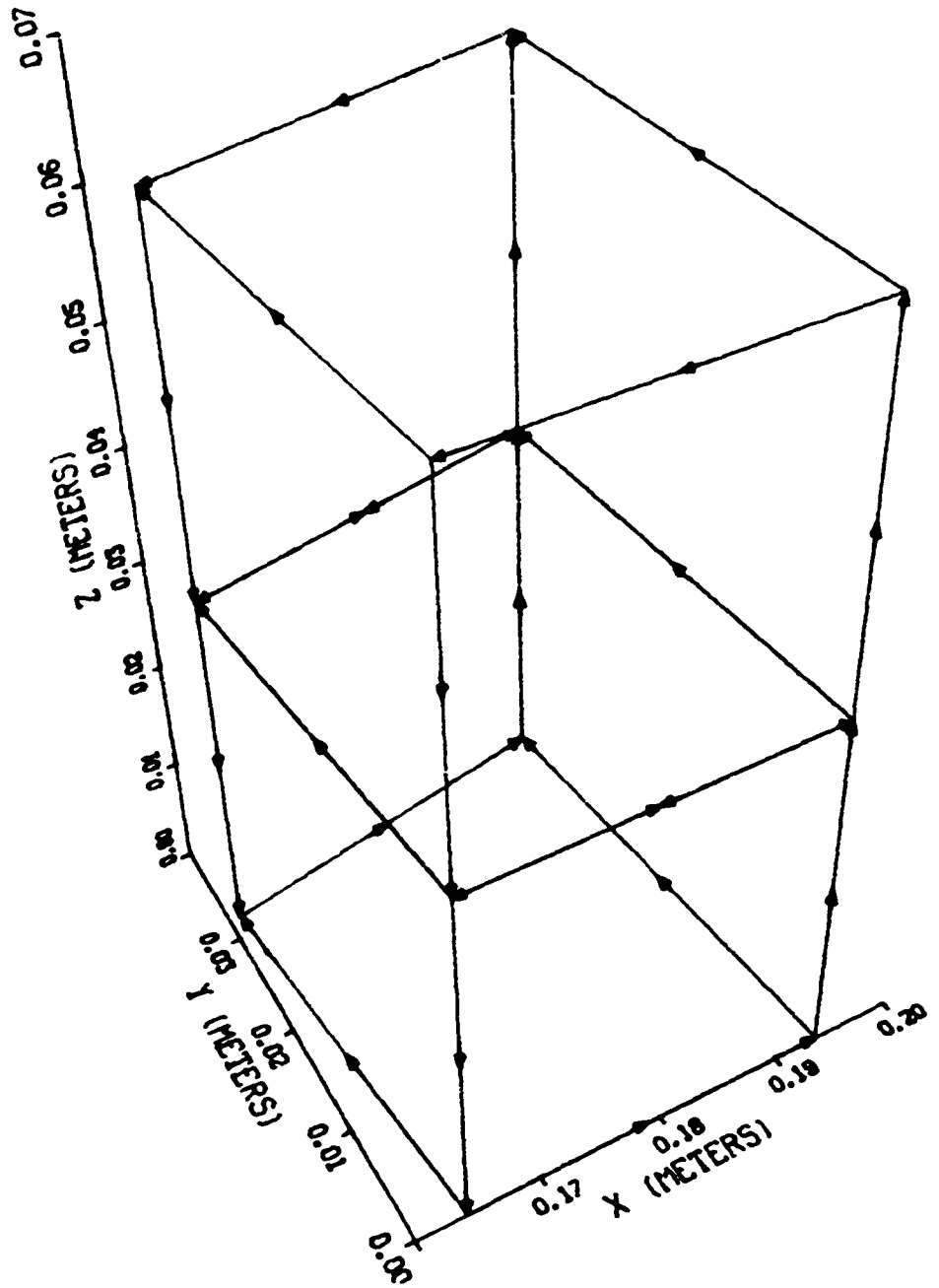

Figure 7. Finite-element idealization of the top half of one stave of the cylinder.

Two lists are generated that will provide MARTSAM with the necessary information to constrain the three-dimensional stave model into a plane (i.e., a two-dimensional axisymmetric model) while still retaining the proper electrical properties for a tangentially polarized, staved cylinder. The BAKADL list sets equal the radial- and vertical-displacement degrees of freedom for nodal points with identical r- and z-coordinates. The MPACKL list packs

out the appropriate radial, azimuthal, and vertical degrees of freedom. In addition, the two lists apply the appropriate electrical-potential boundary conditions. All of the potential degrees of freedom for the nodal points on one side of the stave are set equal to represent the driven foiled surface, and all of the potential degrees of freedom for the nodal points on the opposite side of the stave are set equal to zero to represent the grounded foiled surface. The remaining electrical-potential degrees of freedom are left free and are condensed out later.

The program DATFFC also generates the spherical harmonic transformation matrix [L] and the structure/acoustic fluid coupling matrix [T]. Finally, lists of parameters and matrix sizes are produced for use in both the second and third programs.

PROGRAM MRTFFC*

This instruction program forms and assembles the mass and stiffness matrices of the fluid and for the piezoelectric-ceramic stave, transforms the equations for the stave from rectangular to cylindrical coordinates, constrains the displacement degrees of freedom into an axisymmetric representation, and applies the appropriate displacement and electrical-potential boundary conditions.

Following the procedure given on pages 10, 11, the electrical-potential degrees of freedom are condensed down to the one driving potential. Equations (23) and (24) are then used to calculate the resonance (short circuit) and antiresonance (open circuit) frequencies of the cylinder in air (FREQST and FREQOT). The electrical capacitance (CAP) in air is also calculated from Eq. (30).

The eigenvalues and eigenvectors of the interior problem are calculated from equation (57), and the KAUG lowest eigenfrequencies (FREQY) should contain at least one frequency above the frequency band of interest. Augmenting the surface equation by too many degrees of freedom does no harm except to slightly increase computational costs, but augmentation by too few equations can cause singularity problems.

Finally, the matrices that comprise Eqs. (70) and (74) are assembled for use in the third computer program.

PROGRAM FRQFFC**

This program requires the following input parameters to be specified by the user:

IFFQ, the lowest frequency of interest
ILFQ, the highest frequency of interest
IFQINC, the frequency increment
R(I), distances chosen for the calculation of the transmitting voltage response and/or directivity patterns

---

* MARTSAM program for the analysis of free-flooded cylinders.

** Frequency-sweep computer programs for the analysis of free-flooded cylinders.

Using Eq. (74), the computer program FRQFFC calculates the real and imaginary parts of the electrical impedance Z for each frequency. Also at each frequency, Eq. (78) is used to calculate the radiated power, and then the solution vector is normalized to Z and the transmitting voltage response is calculated from Eqs. (79) and (80) at $\theta = 0$ deg and $\theta = 90$ deg. The 0-deg response is calculated off of the top of the cylinder along its symmetry axis, while the 90-deg response is calculated off of the side of the cylinder on its symmetry plane (see Fig. 5).

Vertical directivity or beam patterns can be calculated for any frequency and distance. Pressures at nodal points that are interior to the fluid-sphere surface and the structural displacements can also be calculated for any frequency. From this data, contour plots can be made of the magnitude and phase of the near-field pressure distribution.

4 EXAMPLE ANALYSES AND COMPARISONS WITH EXPERIMENTS

To assess the accuracy of predications made with the mathematical model presented in this report, three existing free-flooded cylinders were analyzed. These cylinders were chosen because they have quite differenct characteristics, and experimental measurements previously made of the electrical impedance, transmitting voltage response, and directivity patterns were readily available.

Cylinder A is constructed from 32 staves of barium titanate (Ceramic B type) piezoelectric ceramic. To waterproof the bare ceramic element, the cylinder was fiberglass coated. This was done to keep to a minimum the discrepancies between the physical transducer and the mathematical model of the transducer. Except for the waterproof coating, no other additions were made to the bare ceramic element before testing. The agreement between this experiment and the predicted results will be the best possible.

Cylinder B is a 60-stave cylinder constructed from a type of lead zirconate-lead titanate ceramic (a PZT-8 variety). This transducer consists of the ceramic cylinder wrapped with fiberglass to provide mechanical bias that will protect the ceramic from fracture when driven at high levels, inner and outer rubber boots, brass end-rings, and castor oil surrounding the cylinder between the inner and outer rubber boots. (See Fig. 8 for a cross-sectional sketch of a cylinder in a typical case.) The cylinder can now be easily mounted, driven at high levels, and is electrically insulated from the water by the rubber boot and castor oil.

Cylinder C is a 30-stave cylinder constructed from another type of lead zirconate-lead titanate ceramic (a PZT-4 variety). This transducer again was tested with the piezoelectric-ceramic cylinder wrapped in fiberglass and installed in a case similar to the one described for Cylinder B.

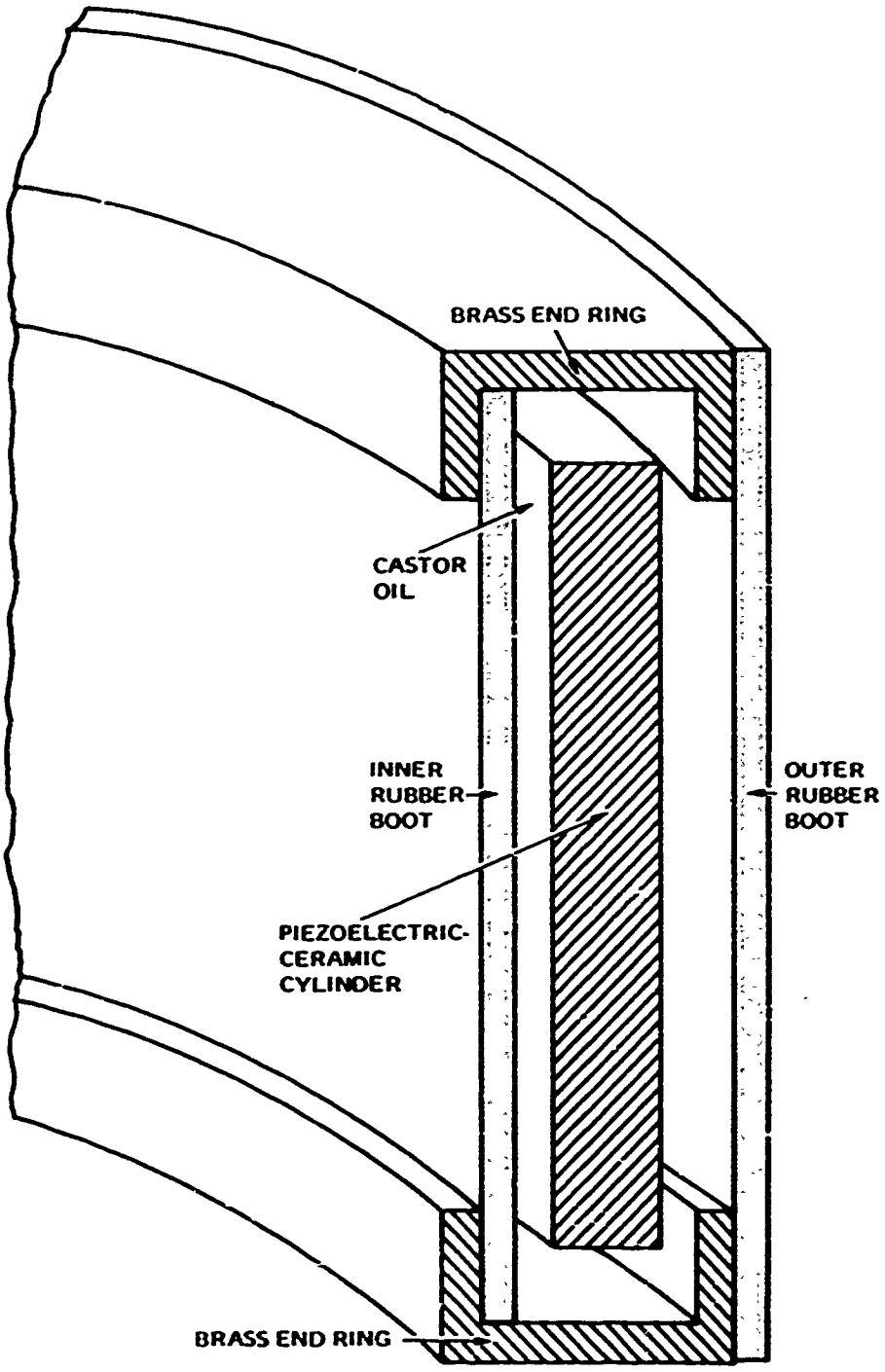

Figure 8. Cross-sectional drawing of a typical free-flooded cylinder transducer in its case, including the ceramic cylinder, brass end rings, inner and outer rubber boots, and castor oil filling of the case.

CYLINDER A

Cylinder A was constructed only for the purpose of comparison with theoretical predictions. The 32-stave barium titanate (ceramic B type) cylinder is not wound with fiberglass filaments nor does it have a protective case or any provision for mounting. Comparisons between experiments conducted with this cylinder and theoretical predictions should yield the best possible agreement.

Table 1 gives some of the parameters used as inputs to the computer programs. As was pointed out in Ref. 11, material parameters that are listed in handbooks (Ref. 29) are often very inaccurate. Ceramic varies from manufacturer to manufacturer, and differences in material parameters as great as 20 percent are not uncommon in supposedly identical types of ceramic. In an attempt to produce material parameters which more accurately describe the ceramic out of which the cylinder under consideration was constructed, a simple perturbation technique was used to fit the breathing resonance, breathing antiresonance, and the electrical capacitance of the cylinder in air. In general, this technique works well. The book and perturbed values for the piezoelectric-ceramic material parameters are listed in Table 2. Table 3 gives the measured values for the electrical capacitance and the first three resonance and antiresonance frequencies of the cylinder in air and also the predicted values on the basis of both the book parameter values and the perturbed parameter values.

Table 1. Input parameters for the three example free-flooded cylinders.

Parameter	Cylinder A	Cylinder B	Cylinder C
RI (m)	0.1641	0.09843	0.08573
RO (m)	0.1927	0.1151	0.09287
RLNTH (m)	0.1272	0.08636	0.07938
NSTAVE	32	60	30
SMALLA (m)	0.22	0.14	0.12
RHO (kg/m^3)	1000	1000	1000
RCV (m/sec)	1500	1500	1500
NPSR	9	9	9
NLR	2	2	2
NTR	1	1	1
NSPHH	10	10	10
KAUG	10	10	10

The measured and predicted real and imaginary parts of the in-water electrical impedance are shown in Fig. 9. The small discrepancies between the computed and the measured responses are attributed to inaccurate material parameters and limitations in the model (inclusion of no material losses and the inability to model glue joints, for example).

Table 2. Book and perturbed piezoelectric-ceramic material parameter values.

Parameter	Cylinder A		Cylinder B		Cylinder C	
	Book*	Perturbed†	Book*	Perturbed	Book*	Perturbed
$\rho(\times 10^3\ kg/m^3)$	5.55	5.55	7.6	7.6	7.5	7.5
s_{11}^E ($\times 10^{-12} m^2/N$)	8.6	9.8	11.1	11.7	12.3	12.7
s_{33}^E ($\times 10^{-12} m^2/N$)	9.1	10.38	13.9	14.6	15.5	16.0
s_{44}^E ($\times 10^{-12} m^2/N$)	22.2	25.3	32.2	33.8	39.0	40.2
s_{12}^E ($\times 10^{-12} m^2/N$)	-2.6	-2.96	-3.7	-3.9	-4.05	-4.17
s_{13}^E ($\times 10^{-12} m^2/N$)	-2.7	-3.08	-4.8	-5.0	-5.31	-5.47
d_{31} ($\times 10^{-12} m/V$)	-58	-55.1	97	-85.8	-123	-110
d_{33} ($\times 10^{-12} m/V$)	149	141.5	225	199	289	258
d_{15} ($\times 10^{-12} m/V$)	242	230	330	292	496	442
ξ_{11}^s/ξ_0	1000	1150	660	654	730	869
ξ_{33}^s/ξ_0	910	1047	600	594	635	756

* See Ref. 29

† See Ref. 11

Table 3. Measured and predicted in-air responses of the three example free-flooded cylinders using book and perturbed piezoelectric material parameter values.

Quantity	Cylinder A			Cylinder B			Cylinder C		
	Measured	Book	Perturbed	Measured	Book	Perturbed	Measured	Book	Perturbed
Capacitance, pf at 1000 Hz	39,000	37,000	38,800	62,970	70,670	62,740	10,021	10,247	10,059
Breathing Resonance, Hz	3,713	3,974	3,721	4,477	4,586	4,476	5,153	5,228	5,146
Breathing Antiresonance, Hz	4,083	4,530	4,087	5,542	5,918	5,489	6,399	7,251	6,517
Bending Resonance, Hz	8,050	8,650	8,100	8,560	8,793	8,583	6,336	6,734	6,628
Bending Antiresonance, Hz	8,050	8,650	8,100	8,560	8,793	8,583	6,310	6,734	6,632
Length Resonance, Hz	17,773	18,871	17,679	20,870	21,610	21,095	21,894	22,567	22,200
Length Antiresonance, Hz	17,803	18,881	17,689	20,970	21,648	21,123	21,968	22,617	22,233

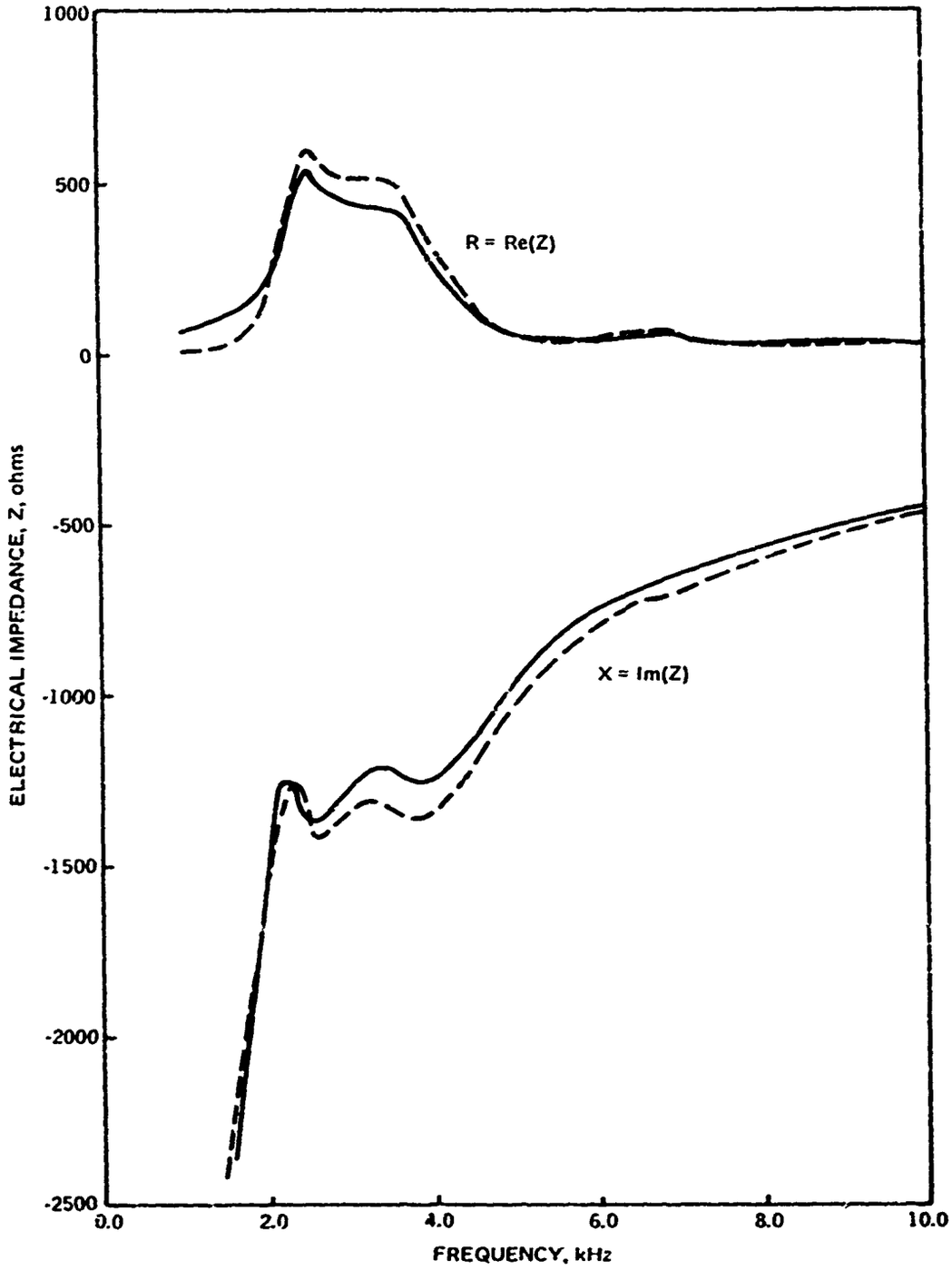

Figure 9. In-water complex electrical impedance of Cylinder A as a function of frequency. Solid lines are for experiment and dashed lines for theory.

The measured and predicted transmitting voltage responses are shown in Fig. 10. The measurements and calculations were made at a distance of 1 m off of the side (θ = 90-deg) of the cylinder. The agreement is again excellent.

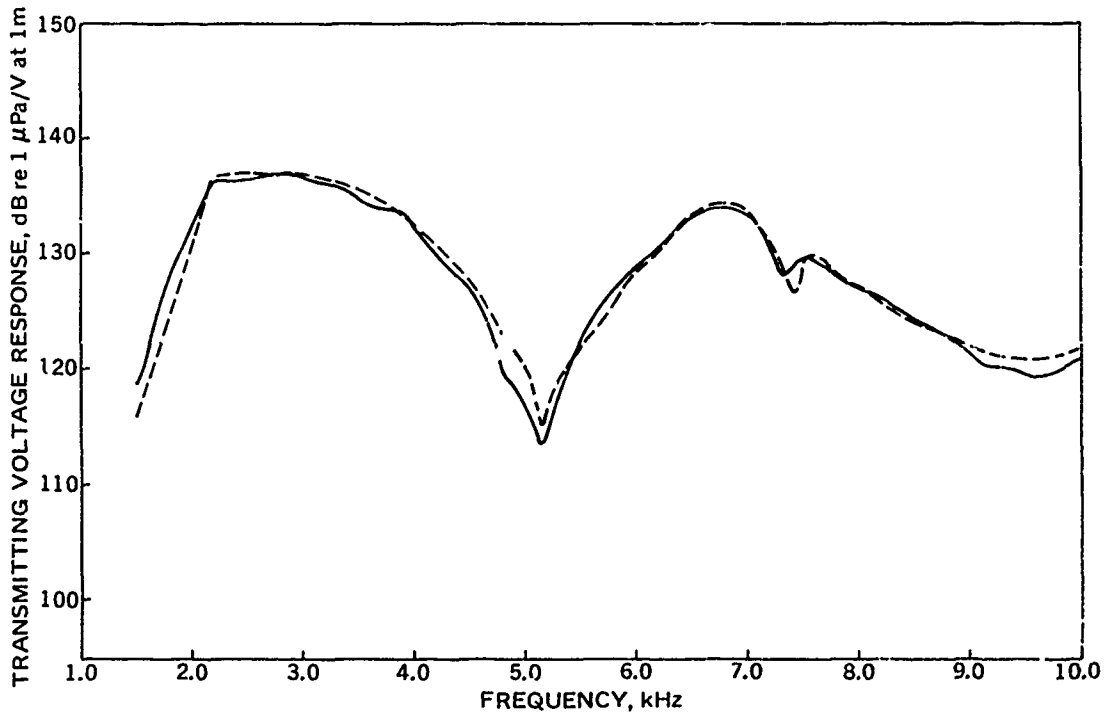

Figure 10. Transmitting voltage response of Cylinder A as a function of frequency. Solid line is for experiment and dashed line for theory.

Figures 11 and 12 display the measured and predicted vertical directivity or beam patterns at 3,000 and 7,000 Hz, respectively.

The maximum source level and maximum radiated power can be calculated by assuming the maximum permissible electrical field will occur for an applied voltage of 5V/0.001 in. (2,000 V/cm, a conservative estimate). For Cylinder A, the minimum distance between adjacent electrodes is 3.2 cm and the maximum voltage is therefore about 6,400 V. At 3,000 Hz, the maximum source level is 213 dB re 1 μPa at 1 m, while at 7,000 Hz, the maximum source level is 210 dB re 1 μPa at 1 m. The minimum source level for the cylinder driven at 6,400 V over the frequency band from 1.5 to 10.0 kHz occurs at about 5,000 Hz and is 190 dB re 1 μPa at 1 m. The maximum radiated power at 3,000 Hz is 6 kW, and the maximum radiated power at 7,000 Hz is 1.7 kW.

CYLINDER B

Cylinder B is constructed from 60 staves of lead zirconate-lead titanate (PZT-8 type) tangentially polarized piezoelectric ceramic. The in-air measurements of the resonance and antiresonance frequencies and electrical capacitance were performed on the bare ceramic element, but the in-water experiments were conducted with the cylinder wrapped in fiberglass

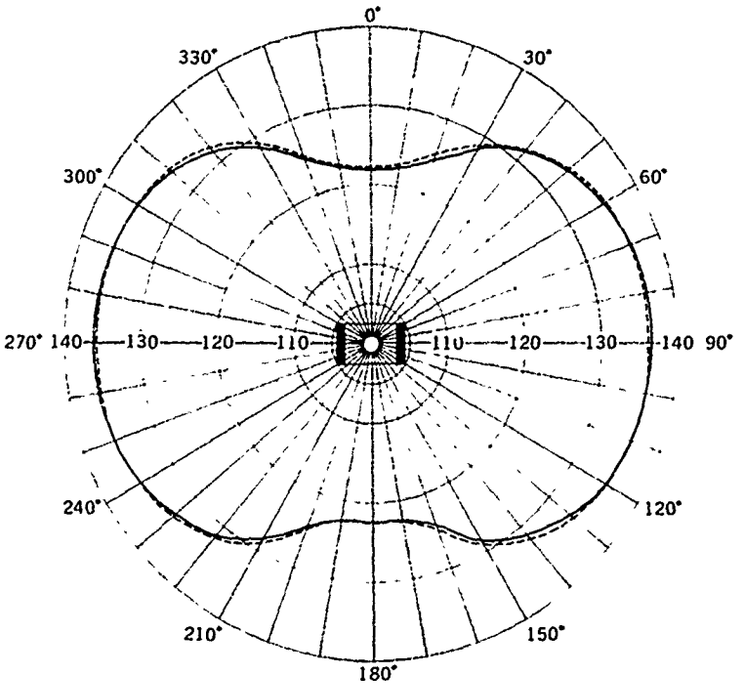

Figure 11. Vertical directivity pattern for Cylinder A at 3,000 Hz. Solid line is for experiment and dashed line for theory. Pressures are plotted in dB re 1 μPa for 1 V input at 1 m.

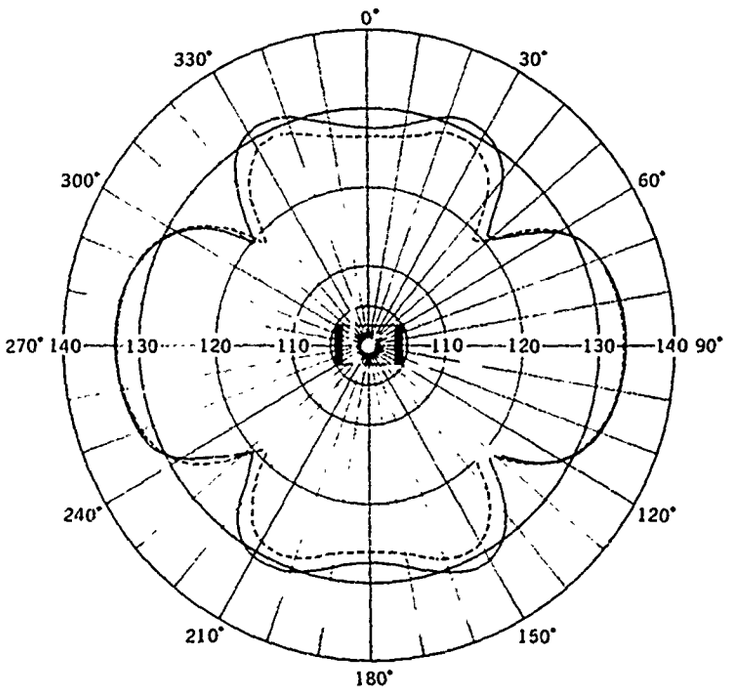

Figure 12. Vertical directivity pattern for Cylinder A at 7,000 Hz. Solid line is for experiment and dashed line for theory. Pressures are plotted in dB re 1 μPa for 1 V input at 1 m.

and mounted in the case shown in Fig. 8. Table 1 gives the dimensions of the ceramic cylinder, Table 2 lists book and perturbed piezoelectric-ceramic material parameters for the PZT-8 like ceramic material, and Table 3 shows the measured and predicted in-air response of the cylinder. Again, the use of perturbed material parameters produces good agreement between theory and experiment.

The measured and predicted real and imaginary parts of the electrical impedance are shown in Fig. 13. The agreement between experiment and theory for this cylinder is not as good as it was for Cylinder A. The presence of the case appears to have two major effects on the response of the transducer. First, the case increases the length of the cylinder, giving the cavity a greater volume; therefore, the first cavity resonance occurs at a lower frequency than predicted. Second, the rubber boots and castor oil introduce larger losses into the system than were present in Cylinder A. Because the mathematical formulation used for these predictions includes no structural damping, at frequencies where losses in the rubber and castor oil are appreciable, the predicted impedance does not compare very well with the measured impedance.

Figure 14 shows the measured and predicted transmitting voltage responses. Again, the lack of damping in the mathematical model and the increase in cavity size cause some discrepancies. In addition, it appears that minor resonances of the case or mounting hardware have been introduced into the system.

Figures 15 and 16 show the measured and predicted vertical directivity patterns at the frequencies of 4,500 and 6,000 Hz, respectively. The agreement of 4,500 Hz is excellent and the agreement at 6,000 Hz is good. The differences in geometry and damping between the bare ceramic cylinder and the transducer as tested appear to produce the greatest effect off of the top of the cylinder (for small angles of θ).

The maximum source level and maximum radiated power can be calculated in the same manner used for Cylinder A. Assuming a maximum voltage of 2,000 V the maximum source level is approximately 206 dB re 1 μPa at 1 m at 4,000 Hz and 193 dB re 1 μPa at 1 m at 8,000 Hz. The maximum radiated power at 3,000 Hz is 5 kW, at 4,000 Hz is 1 kW, and at 8,000 Hz is about ½ kW.

CYLINDER C

Cylinder C is a 30-stave cylinder constructed from lead zirconate-lead titanate (PZT-4 type) piezoelectric ceramic with the dimensions given in Table 1. The in-air measurements of the resonance and antiresonance frequencies and electrical capacitance were performed on a bare ceramic element, and quite interesting results were found. From Table 3, the measured in-air response of the transducer shows that the bending resonance and antiresonance frequencies lie between the breathing resonance frequency and the breathing antiresonance frequency. This was verified by using an optical probe to measure the displacement distribution along the length of the cylinder at the frequencies of interest. The calculated in-air response made with book material parameter values also predicted this phenomenon but not at the correct frequencies. Performing the same simple three-parameter

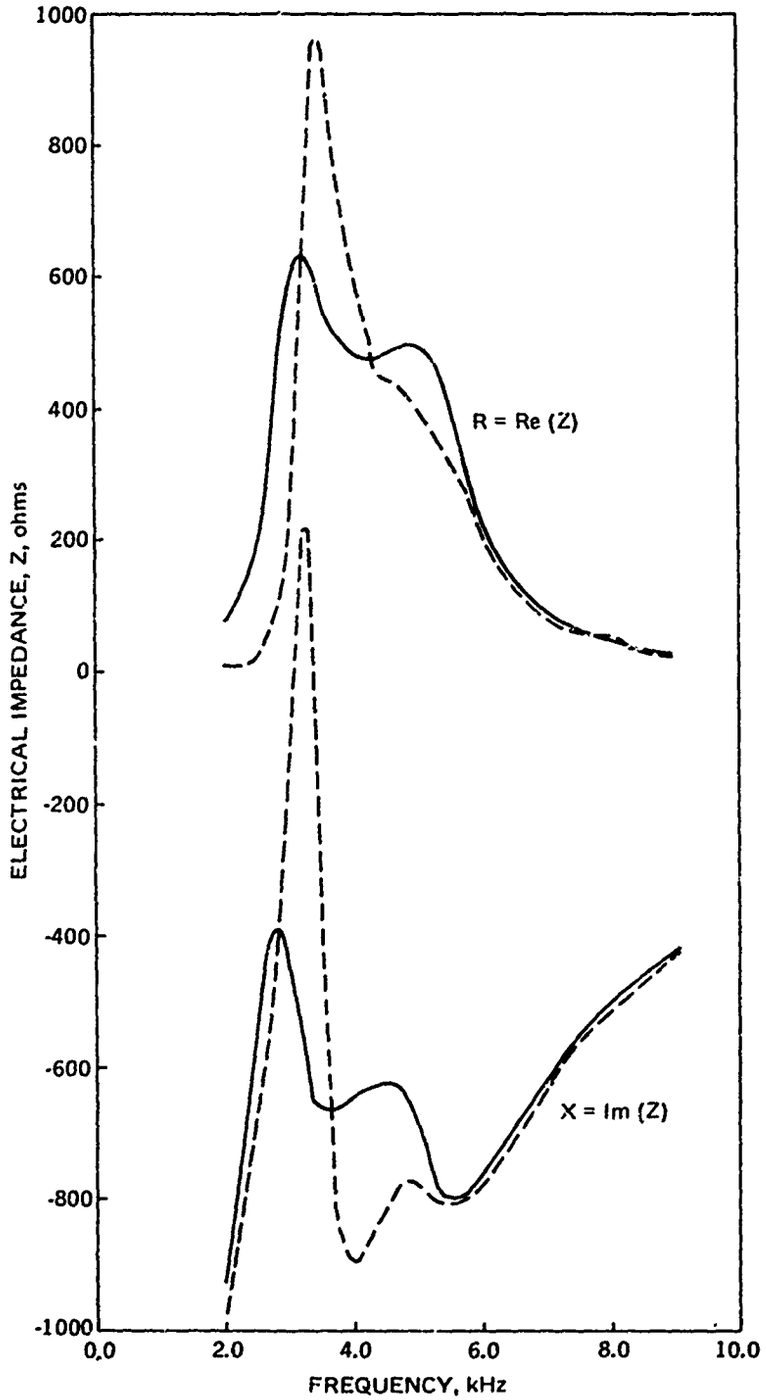

Figure 13. In-water complex electrical impedance of Cylinder B as a function of frequency. Solid lines are for experiment and dashed lines for theory.

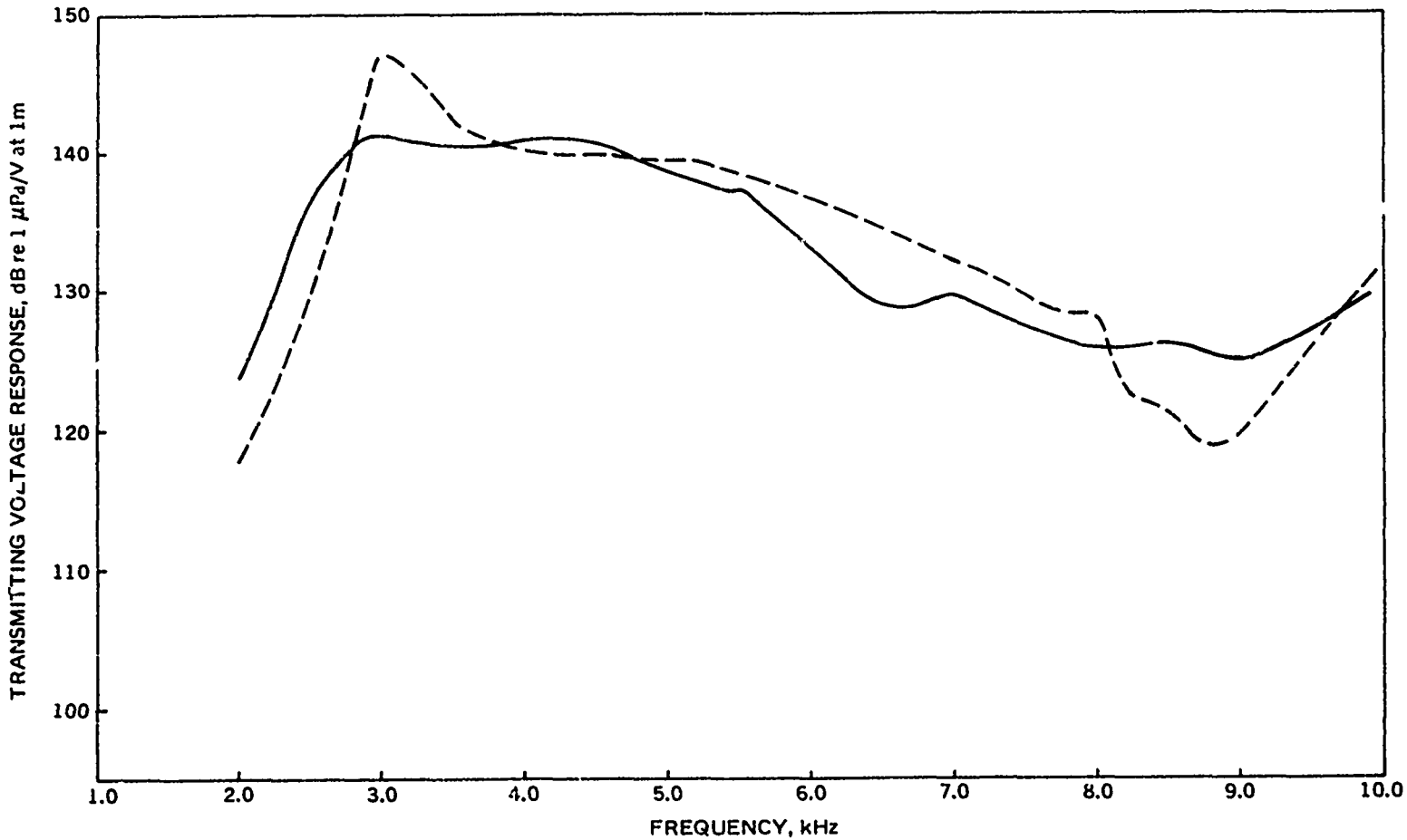

Figure 14. Transmitting voltage response of Cylinder B as a function of frequency. Solid line is for experiment and dashed line for theory.

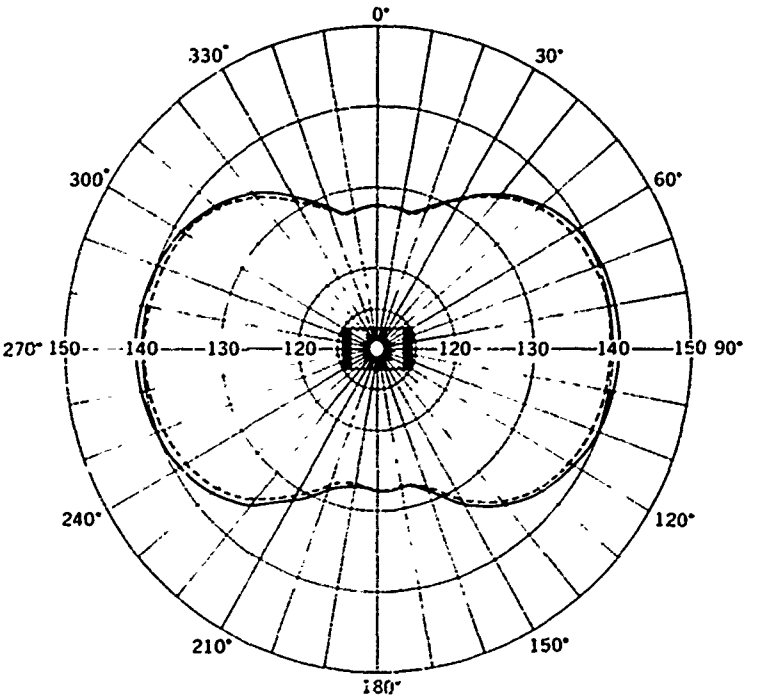

Figure 15. Vertical directivity pattern for Cylinder B at 4,500 Hz. Solid line is for experiment and dashed line for theory Pressures are plotted in dB re 1 μPa for 1 V input at 1 m.

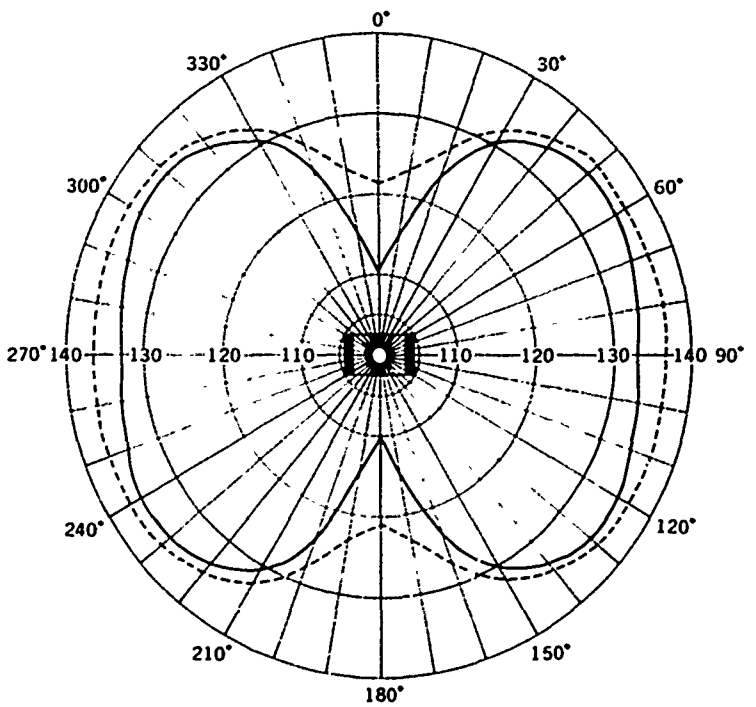

Figure 16. Vertical directivity pattern for Cylinder B at 6,000 Hz. Solid line is for experiment and dashed line for theory. Pressures are plotted in dB re 1 μPa for 1 V input at 1 m.

perturbation calculation that was performed for Cylinders A and B resulted in only a partial success. The calculated resonance and antiresonance frequencies more closely fitted the measured frequencies, but the bending resonance and antiresonance frequencies no longer lay between the breathing resonance frequency and the breathing antiresonance frequency. It appears that either the simple perturbation calculation performed here is not sufficient to fit all of the material parameters or the finite-element model of the cylinder has too few elements to predict the proper bending. However, this discrepancy in frequencies is only about 5 percent and should not affect the in-water response of the transducer. Table 2 gives the book and perturbed piezoelectric-ceramic material parameter values.

Figure 17 shows the measured and predicted real and imaginary parts of the electrical impedance. The experiment was performed with the ceramic cylinder again housed in a case similar to Fig. 8. The predicted impedance closely follows that measured experimentally except at the two frequencies where again damping flattens the measured response.

The measured and predicted transmitting voltage response for Cylinder C is shown in Fig. 18. Except for the overestimation of the level at the cavity resonance frequency, the two curves show excellent agreement.

Figures 19, 20 and 21 display the measured and predicted vertical directivity patterns at 3,000, 6,000 and 10,000 Hz, respectively. Just as for the previous cylinder housed in a case, the measured and predicted patterns do not agree as well at $\theta = 0$ deg, as they do at $\theta = 90$ deg. The added structure and the presence of structural damping give the transducer a response that is slightly altered from that of the bare ceramic elements.

The maximum source level and maximum radiated power are found by assuming a maximum voltage of 3,500 V. The maximum source level is therefore, for example, 203 dB re 1 μPa at 1 m at 3,500 Hz and falls to only 197 dB re 1 μPa at 1 m at 8,000 Hz. The maximum radiated power is 7.4 kW at 3,000 Hz but down to 0.4 kW at 5,750 Hz and to 0.2 kW at 8,000 Hz. These are again conservative figures since acceptable drive levels are often 6 or 8 V per 0.001 in.

5 CONCLUSIONS

The powerful mathematical modeling techniques that have been presented in this report can be used to calculate the response of any axisymmetric transducer (or transducer that can be approximated by an axisymmetric representation over the frequency band of interest) when immersed in an infinite acoustic fluid medium. In particular, this report describes the computer programs that have been written to use this mathematical formulation in the analysis of tangentially polarized piezoelectric-ceramic, free-flooded cylinder transducers. The programs are designed to take a few basic parameters and produce a set of graphs that display the complex electrical impedance, transmitting voltage response, and radiated power as functions of frequency. At any selected frequency, the vertical directivity pattern (the horizontal directivity pattern is always circular since an axisymmetric response is assumed) and displacement distribution on the cylinder can be calculated.

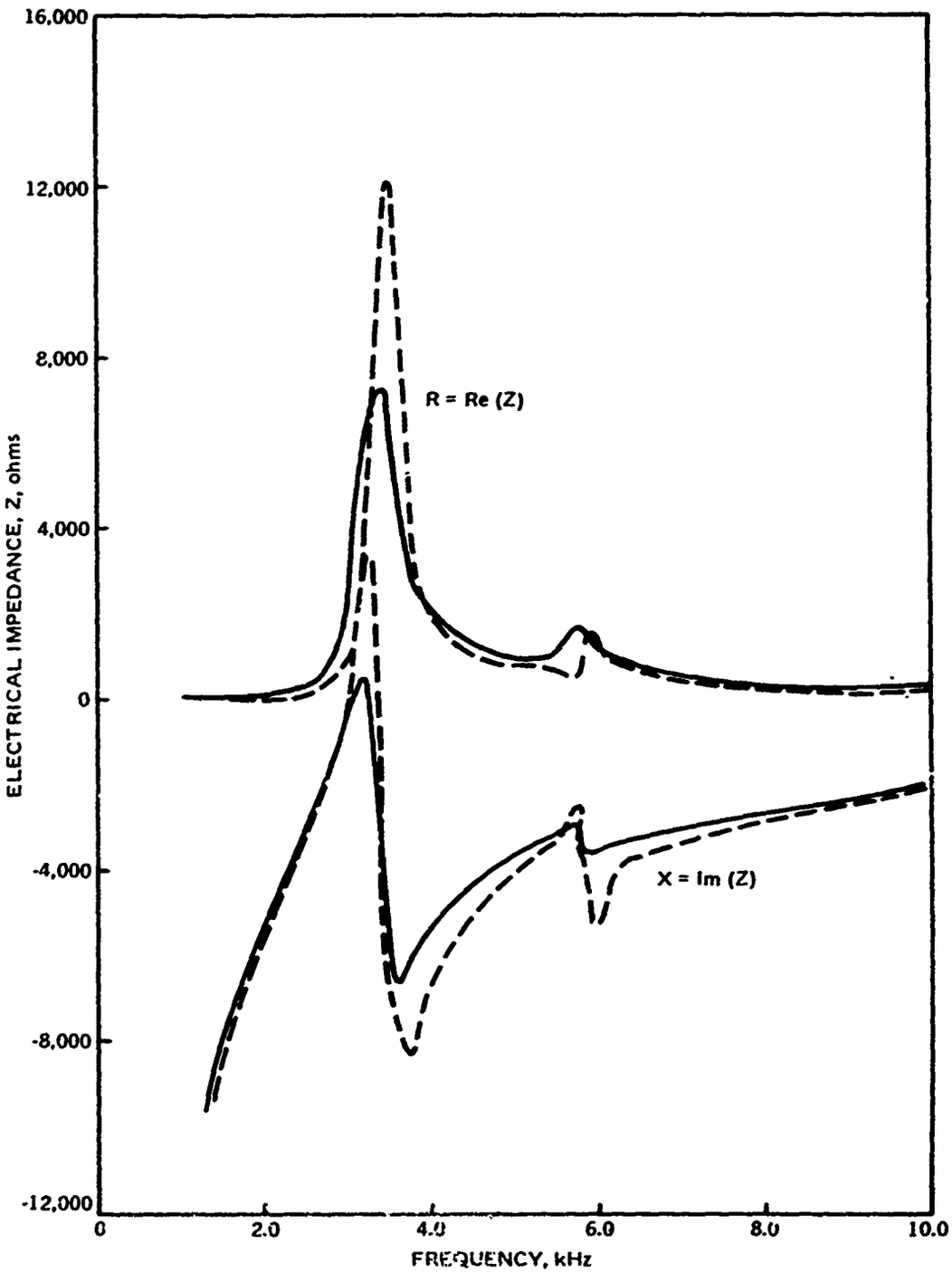

Figure 17. In-water complex electrical impedance for Cylinder C as a function of frequency. Solid lines are for experiment and dashed lines for theory.

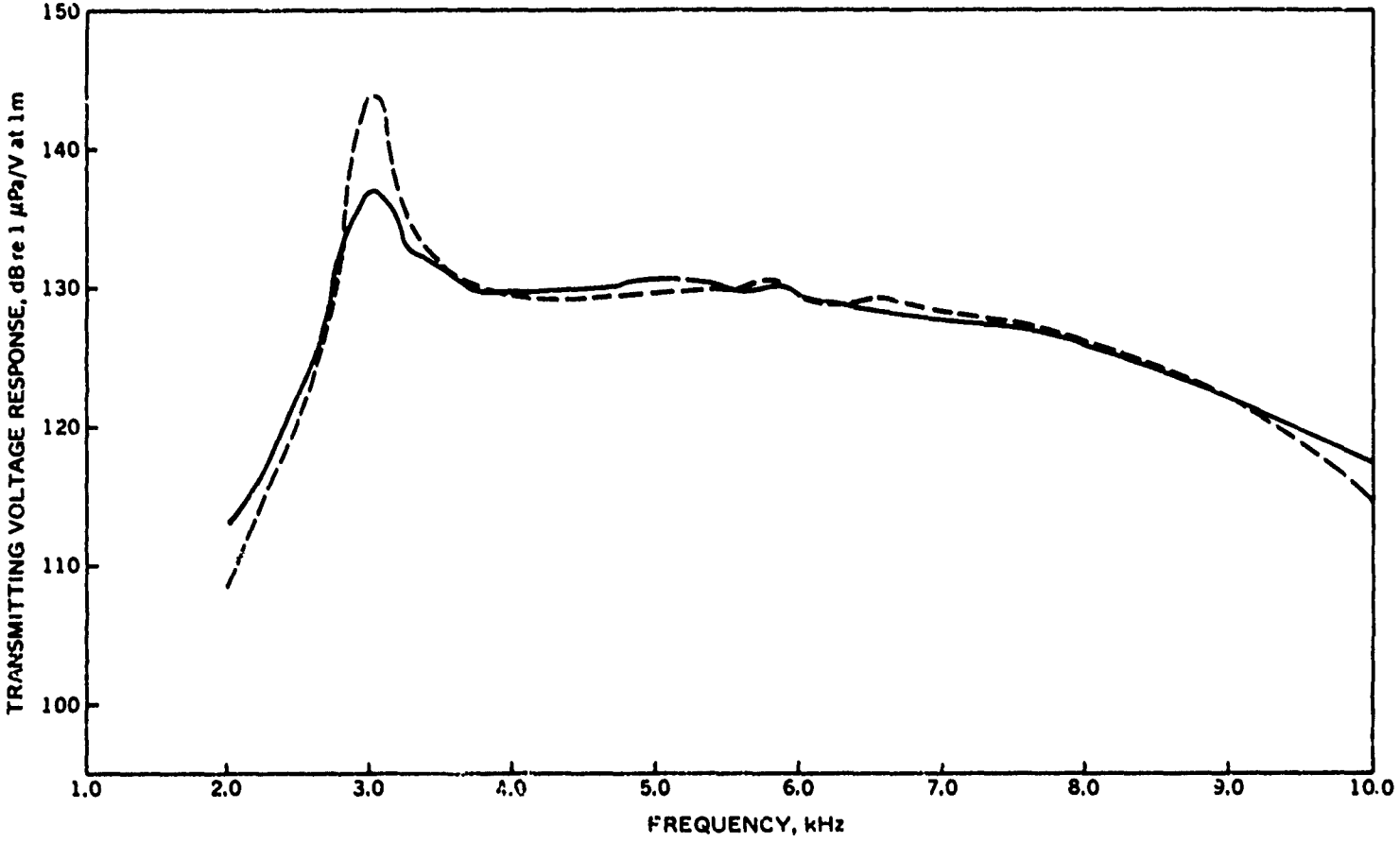

Figure 18. Transmitting voltage response of Cylinder C as a function of frequency. Solid line is for experiment and dashed line for theory.

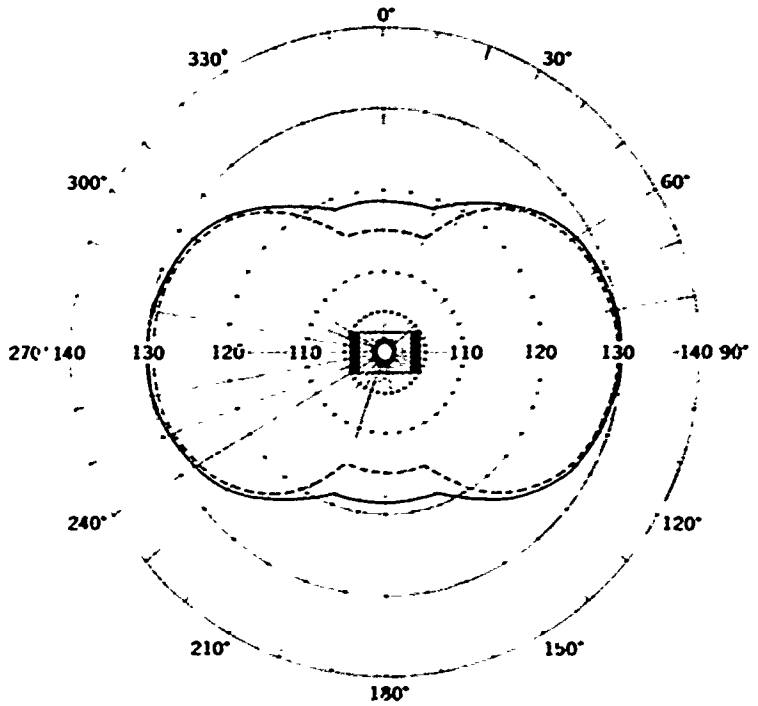

Figure 19. Vertical directivity pattern for Cylinder C at 4,000 Hz. Solid line is for experiment and dashed line for theory. Pressures are plotted in dB re 1 μPa for 1 V input at 1 m.

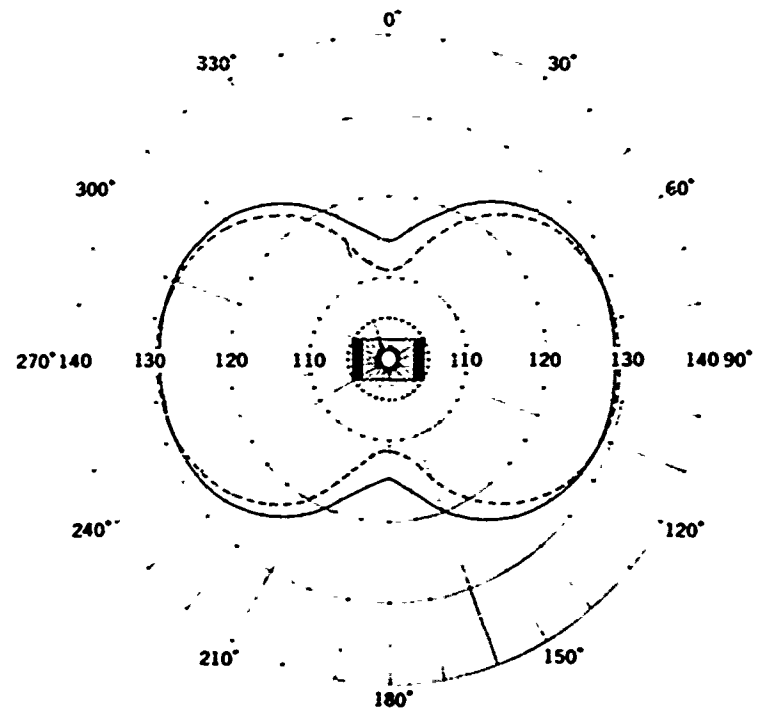

Figure 20. Vertical directivity pattern for Cylinder C at 6,000 Hz. Solid line is for experiment and dashed line for theory. Pressures are plotted in dB re 1 μPa for 1 V input at 1 m.

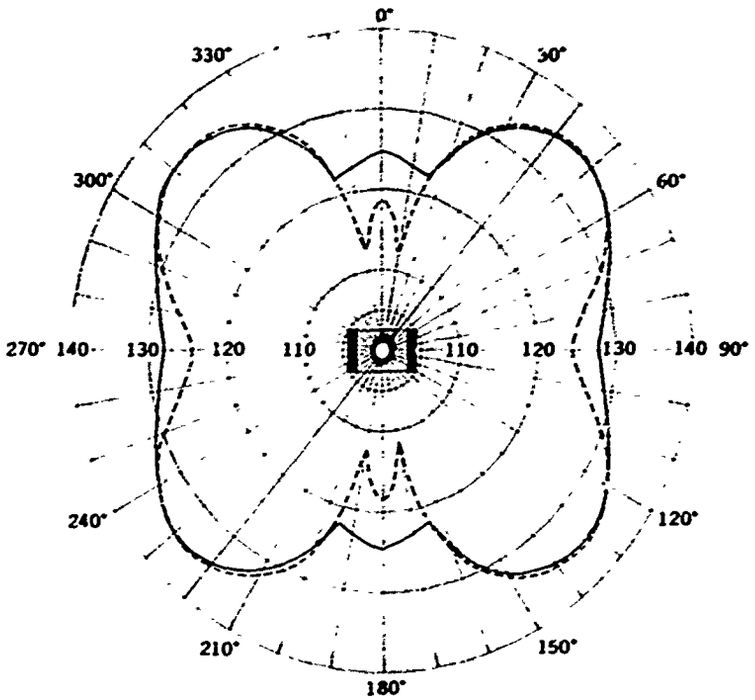

Figure 21. Vertical directivity pattern for Cylinder C at 10,000 Hz. Solid line is for experiment and dashed line for theory. Pressures are plotted in dB re 1 μPa for 1 V input at 1 m.

Three free-flooded cylinders were analyzed and the results compared with experiment. The first experiment was designed to approximate as closely as possible the transducer that was mathematically modeled. No fiberglass wrapping or transducer case was employed. The comparison between theory and experiment for this cylinder is excellent at all frequencies.

The agreement between theory and experiment for the other two examples is no longer excellent, but the predictions are still good over a broad frequency band. The assumptions in the mathematical model remain the same; i.e., no structural damping and no case. The transducer used in the experiments, however, consists of the piezoelectric-ceramic cylinder enclosed between inner and outer rubber boots and brass end rings and filled with castor oil. This additional structure increases the minimal damping that exists for the ceramic cylinder to a significant amount.

In addition to the structural damping (particularly in the rubber boots and castor oil), the added structure makes its own contribution to the produced pressure field. Since the model includes none of this added structure, it cannot predict the scattering from the case of the pressure field produced by the ceramic cylinder.

These deficiencies are not considered to be serious. If more exact predictions are needed, future mathematical modeling efforts can be directed toward modeling of the complete transducer, including the brass end rings, castor oil, and rubber boots. Structural damping may also be included in the model. These improvements should pose no great

mathematical modeling difficulties but would increase computational costs. At present computer rates, the minimum total cost to operate the computer programs described in this report is approximately $125. This high cost for the analysis of each proposed free-flooded cylinder limits the design capabilities of the model. However, as a final check or a last iteration on a set of dimensions chosen by some simpler and more economical means, the mathematical modeling techniques described in this report offer predictions that are nearly as accurate as experimental measurements and are much cheaper and faster.

6 REFERENCES

1. C. E. Green, "Mosaic Construction for Electroacoustical Cylindrical Transducers," United States Patent 3,177,382 (6 April 1965).

2. M. C. Junger, "Sound Radiation from a Radially Pulsating Cylinder of Finite Length," Harvard Univ. Acoust. Res. Lab. (24 June 1955).

3. C. V. Stephenson, "Radial Vibrations in Short, Hollow Cylinders of Barium Titanate," J. Acoust. Soc. Am. 28, 51-56 (1956).

4. J. F. Haskins and J. L. Walsh, "Vibrations of Ferroelectric Cylindrical Shells with Transverse Isotropy," J. Acoust. Soc. Am. 29, 729-734 (1957).

5. G. A. Brigham and M. F. Borg, "An Approximate Solution to the Acoustic Radiation of a Finite Cylinder," J. Acoust. Soc. Am. 32, 971-981 (1960).

6. M. C. Junger, "A Variational Solution of Solid and Free-Flooding Cylindrical Sound Radiators of Finite Length," Cambridge Acoust. Assoc. Tech Rept. U-177-48 (1 March 1964).

7. G. W. McMahon, "Performance of Open Ferroelectric Ceramic Cylinders in Underwater Transducers," J. Acoust. Soc. Am. 36, 528-533 (1964).

8. W. Williams, N. G. Parke, D. A. Moran and C. H. Sherman, "Acoustic Radiation from a Finite Cylinder," J. Acoust. Soc. Am. 36, 2316-2322 (1964).

9. D. T. Porter, "Method for Computing the Electrical and Acoustical Behavior of Free-Flooding Cylindrical Transducer Arrays," J. Acoust. Soc. Am. 44, 514-522 (1968).

10. J. T. Hunt, "Modeling Complex Motions of Sonar Transducers by the Finite Element Method," Independent Research and Independent Exploratory Development Annual Report - 1972, Naval Undersea Center Technical Publication 319, August 1972.

11. R. R. Smith, J. T. Hunt, and D. Barach, "Finite Element Analysis of Acoustically Radiating Structures with Applications to Sonar Transducers," J. Acoust. Soc. Am. 54, 1277-1288 (1973).

12. H. A. Schenck, "Improved Integral Formulation for Acoustic Radiation Problems," J. Acoust. Soc. Am. 44, 41-58 (1968).

13. J. T. Hunt, M. R. Knittel and D. Barach, "A Finite Element Approach to Acoustic Radiation from Elastic Structures," J. Acoust. Soc. Am. 55, 269-280 (1974).

14. O. C. Zienkiewicz, The Finite Element Method in Engineering Science (McGraw-Hill, London, 1971), 2nd Edition.

15. J. S. Przemieniecki, Theory of Matrix Structural Analysis (McGraw-Hill, New York, 1968).

16. H. Allik, et al., "GENSAM, A General Structural Analysis and Matrix System," General Dynamics/Electric Boat Division Report P411-70-009 (March 1970).

17. O. C. Zienkiewicz and R. E. Newton, "Coupled Vibrations of a Structure Submerged in a Compressible Fluid," Proceedings of the International Symposium on Finite Element Techniques, Int. Assoc. for Ship Structures, Stuttgart, Germany (10-12 June 1969).

18. H. Allik, "Formulation of Acoustic Fluid Finite Elements," General Dynamics/Electric Boat Division Technical Note, written under Naval Undersea Center purchase order no. N66001-72-6010U0140 (5 May 1972).

19. H. Allik and T. J. R. Hughes, "Finite Element Method for Piezoelectric Vibrations," Intern. J. Num. Meth. Eng. 2, 151-157 (1970).

20. L. G. Copely, "Fundamental Results Concerning Integral Representations in Acoustic Radiation," J. Acoustic. Soc. Am. 44, 22-32 (1968).

21. C. H. Wilcox, "A Generalization of Theorems of Rellich and Atkinson," Proc. Am. Math. Soc. 7, 271-276 (1956).

22. B. B. Baker and E. T. Copson, The Mathematical Theory of Huygen's Principle (The Clarendon Press, Oxford, England, 1950), 2nd Edition.

23. L. H. Chen and D. G. Schweikert, "Sound Radiation from an Arbitrary Body," J. Acoust. Soc. Am. 35, 1626-1632 (1963).

24. G. Chertock, "Sound Radiation from Vibrating Surfaces," J. Acoust. Soc. Am. 36, 1305-1313 (1964).

25. A. Messiah, Quantum Mechanics, Volume 1 (John Wiley and Sons, New York, 1962), p. 494.

26. See reference 25, p. 489.

27. J. T. Hunt and C. Johnson, "Free Vibrations of a Tangentially Polarized Piezoelectric Cylinder," July 1972, unpublished.

28. R. R. Smith, "An Algorithm for Plotting Contours in Arbitrary Planar Regions," Naval Undersea Center Technical Publication 267, October 1971.

29. "Piezoelectric Technology Data for Designers," Clevite Corp., Piezoelectric Division (now Vernitron, Piezoelectric Division), Bedford, Ohio (1965).